Post-outburst Evolution of Bona Fide FU Ori-type V2493 Cygnus: A Spectro-photometric Monitoring

Arpan Ghosh[1,2] , Saurabh Sharma[1] , Joe P. Ninan[3] , Devendra K. Ojha[3] , Bhuwan C. Bhatt[4], D. K. Sahu[4] , Tapas Baug[5] ,
R. K. Yadav[6], Puji Irawati[6] , A. S. Gour[2], Neelam Panwar[1] , Rakesh Pandey[1,2] , Tirthendu Sinha[5,7] , and
Aayushi Verma[1]

[1] Aryabhatta Research Institute of Observational Sciences (ARIES), Manora Peak, Nainital 263001, India; arpan@aries.res.in
[2] School of Studies in Physics and Astrophysics, Pandit Ravishankar Shukla University, Raipur 492010, Chhattisgarh, India
[3] Department of Astronomy and Astrophysics, Tata Institute of Fundamental Research (TIFR), Mumbai 400005, Maharashtra, India
[4] Indian Institute of Astrophysics, II Block, Koramangala, Bangalore 560034, India
[5] Satyendra Nath Bose National Centre for Basic Sciences (SNBNCBS), Salt Lake, Kolkata 700 106, India
[6] National Astronomical Research Institute of Thailand (Public Organization), 260 Moo 4, T. Donkaew, A. Maerim, Chiangmai, 50180, Thailand
[7] Kumaun University, Nainital 263001, India

Abstract

We present here the results of 8 yr of our near-simultaneous optical–near-infrared spectro-photometric monitoring of the bona fide FU Ori (FUor)-type candidate V2493 Cygnus (V2493 Cyg) starting from 2013 September to 2021 June. During our optical monitoring period (between 2015 October 16 and 2019 December 30), the V2493 Cyg is slowly dimming with an average dimming rate of $\sim 26.6 \pm 5.6$ mmag yr^{-1} in the V band. Our optical photometric colors show a significant reddening of the source post the second outburst pointing toward a gradual expansion of the emitting region post the second outburst. The mid-infrared colors, on the contrary, exhibit a blueing trend, which can be attributed to the brightening of the disk due to the outburst. Our spectroscopic monitoring shows a dramatic variation of the Hα line as it transitioned from absorption feature to the emission feature and back. Such transition can possibly be explained by the variation in the wind structure in combination with accretion. Combining our time evolution spectra of the Ca II infrared triplet lines with the previously published spectra of V2493 Cyg, we find that the accretion region has stabilized compared to the early days of the outburst. The evolution of the O I $\lambda 7773$ Å line also points toward the stabilization of the circumstellar disk post the second outburst.

1. Introduction

Enhanced episodic accretion (or outburst) is an important phenomenon in the evolution of a low-mass star (mostly $\leqslant 1\,M_\odot$, and in some systems 2–3 $M_\odot$, Hartmann et al. 2016) spanning from the embedded protostars to the main-sequence (MS) stages (Audard et al. 2014). The timescale of these outbursts ($\sim$months to decades) is very short if we compare it to the millions of years spent on the formation stages or billions of years spent on the MS stages of the low-mass stars. This makes these events extremely rare. However, according to Scholz et al. (2013), each low-mass star is expected to experience statistically $\sim$50 short duration outbursts anytime during their early pre-main-sequence (PMS) stages, i.e., Class 0 and Class II stages (see also, Safron et al. 2015). Though, these outbursts are small in temporal scales, but are capable of delivering significant fraction of mass from the circumstellar disk onto the central PMS star (Vorobyov & Basu 2006). The episodically accreting young stars are broadly classified into two groups, i.e., FU Ori types (FUors) and EX Lupi types (EXors), which usually show a brightening of 4–5 mags (lasting for several decades) and 2–3 mags (spanning for few months to few years), respectively, in optical wavelengths. The

FUors show only absorption lines in their spectra, whereas the EXors show mostly emission lines (Hartmann & Kenyon 1996; Hartmann 1998). Because of the rarity of the outburst events, the physical origin behind the enhanced accretion rates in the low-mass PMS stars is not fully understood. In recent times, various models have been proposed to explain this, e.g., thermal instability, magnetorotational instability, combination of magnetorotational instability and gravitational instability, disk fragmentation, external perturbations, etc. (see, for details, Audard et al. 2014). Thus, a continuous spectroscopic and photometric monitoring of the evolution of the outburst sources can provide important insights on these models on enhanced accretion in the life of low-mass PMS stars.

V2493 Cygnus (V2493 Cyg; $\alpha_{\rm J2000} = 20^{\rm h}58^{\rm m}16\overset{\rm s}{.}90$, $\delta_{\rm J2000} = +43°53'42\overset{''}{.}8$; $l = 85.113248°$, $b = -1.200676°$) is one such source, categorized as a bona fide FUor Miller et al. (2011), located in the dark cloud known as the "Gulf of Mexico" in the Cygnus star-forming arm of our Galaxy. The name V2493 Cyg was designated by the General Catalog of Variable Stars (Kazarovets et al. 2011). It is also referred to as HBC 722 (Herbig & Bell 1988), LkHA 188-G4 (Cohen & Kuhi 1979), and PTF10qpf based on the identification of the source by Palomar Transient Factory (PTF; Miller et al. 2011). Henceforth, we will use the name V2493 Cyg throughout this paper to designate this source. The distance of this source was previously estimated as 520 ± 50 pc (Laugalys et al. 2006;
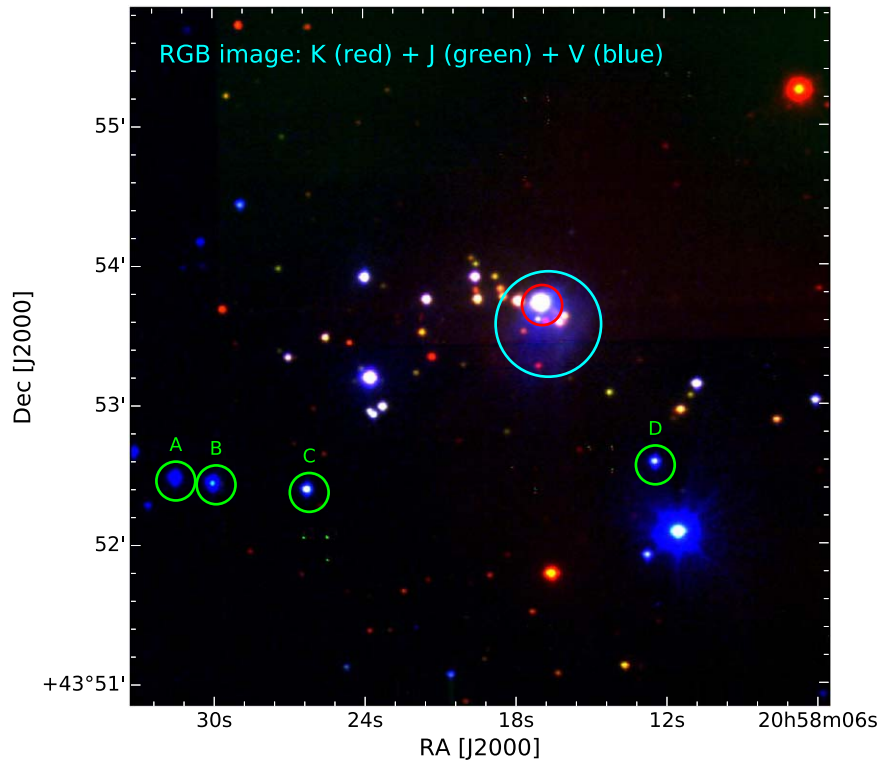
Figure 1. Red giant branch color composite image of V2493 Cyg obtained by using the TIRSPEC K_s (red), J (green), and 1.3 m DFOT V (blue) band images. The source V2493 Cyg is marked by a red circle. The cyan circle marks the extent of the reflection nebula that first appeared after the first outburst and has remained until date. The local standard stars that have been used for calibration of V2493 Cyg are marked by green circles.

Green et al. 2013). However, from the precise parallax measurements of Gaia Data Release 3 (DR3; Bailer-Jones et al. 2021), this source is found to be located at a distance of 760 ± 8 pc. Henceforth, we will adopt the distance obtained using Gaia DR3. From the shape of the spectral energy distribution (SED), Kóspál et al. (2011), Miller et al. (2011) have shown that the V2493 Cyg was a Class II young stellar object (YSO) before it transitioned to its first outburst stage. V2493 Cyg experienced its first outburst during the summer of 2010. It reached its maximum brightness in September 2010 with $\Delta V \sim 4\overset{.}{.}7$ mag (Semkov et al. 2010). It then started to fade, reaching an intermediate quiescent stage in 2011 October ($\Delta V \sim 1\overset{.}{.}45$ mag from the initial outburst peak). Subsequently, it again started to brighten, reaching a maximum brightness in 2012 April with $\Delta V \sim 3\overset{.}{.}3$ mag (Semkov et al. 2012). Post the second outburst, Green et al. (2013) and Baek et al. (2015) investigated for periodicity in V2493 Cyg. They have found periods of ~ 6 and ~ 10 days. They attributed these periodicities to the rotating clumps in the disk. Lee et al. (2015) studied the evolution of V2493 Cyg using its high resolution spectra taken between 2010 December and 2014 November. They have found evidence of the wind driven by the accretion in V2493 Cyg. Their monitoring also revealed an anticorrelation between the spectroscopic features originating from the disk and from the wind. They have attributed this to the possible rebuilding of the inner disk. The extent of the disk at optical and near-infrared (NIR) wavelengths was found to be 39 $R_\odot$ and 76 $R_\odot$, respectively, using the optical and NIR spectra. Kóspál et al. (2016) performed a detailed modeling of the 2010 and 2011 outburst of V2493 Cyg based on their detailed optical, NIR, and millimeter monitoring and spectroscopic observations. Their investigation revealed that the initial outburst of 2010 was powered by the rapid infall of piled-up material from the innermost part of the disk onto the star. The 2011 outburst was

believed to be due to a slower ionization front that started to expand outward. The study also demonstrated that episodic accretion can be observed in young stellar objects with very-low-mass disks.

Since the year 2013, no detailed investigation on V2493 Cyg has been carried out, which is still in the second outburst stage. Thus, a long-term monitoring of V2493 Cyg can help us characterize the complex physical processes going on in this current evolutionary stage. We have monitored V2493 Cyg from 2013 September to 2021 June, both photometrically and spectroscopically in optical to NIR wavelengths, using different telescopes. Figure 1 shows the color composite image of V2493 Cyg generated from our observations during our monitoring period. A reflection nebula appeared after the first outburst, which obscured V2493 Cyg at optical wavelengths. The source is visible at NIR K_s band whereas the extent of the reflection nebula is traced out by the optical V band as shown in Figure 1. We have combined our results with the previously published results. This helps us to provide further insights on the nature of these types of sources. In Section 2, we describe the details of the observations and the techniques employed in the data reduction. In Section 3, we describe the photometric and spectrometric evolution of V2493 Cyg during our monitoring period. In Section 4, we explain the evolution of V2493 Cyg based on various physical models and conclude our study at the end.

2. Observation and Data Reduction

2.1. Photometric Data

2.1.1. Present Data

We have observed V2493 Cyg in optical broadband V, $\boldsymbol{R}_C$, and I_C Johnson–Cousins filters using the ANDOR 512×512

and ANDOR 2k × 2k CCD cameras on the 1.3 m Devasthal Fast Optical Telescope (DFOT) of Aryabhatta Research Institute of Observational Sciences (ARIES)[8] and the Hanle Faint Object Spectrograph Camera (HFOSC) of 2 m Himalayan Chandra Telescope (HCT)[9] at Hanle, India. In the NIR wavelengths, we have observed V2493 Cyg in J, H, and K_S bands using the TIFR Near Infrared Spectrometer and Imager (TIRSPEC) mounted on HCT (Ninan et al. 2014). Table 1 provides the complete log of observations. We have photometrically observed V2493 Cyg at 70 different epochs between 2013 and 2019 with 26 epochs using the 1.3 m DFOT (optical bands), 16 epochs using HFOSC (optical bands), and 28 epochs using the TIRSPEC on 2 m HCT (NIR bands).

For the image processing, we have used the standard procedures as outlined in Sharma et al. (2020). As V2493 Cyg is surrounded by a reflection nebula, point-spread function photometry does not fully remove the inter-night nebular contamination. Therefore, we have followed the approach of Ninan et al. (2013) by which they did photometry of another similar FUor and/or EXor source "V1647 Ori," which is also surrounded by a nebula. In the case of V1647 Ori, it was found out that there is a strong correlation between fluctuation in magnitude with that of atmospheric seeing. This resulted from the contamination of the nebular flux into the aperture of V1647 Ori which is a function of atmospheric seeing. Briefly, we have generated a set of images for each night by convolving each frame with a two-dimensional Gaussian kernel of different standard deviations to simulate different atmospheric seeing conditions. The magnitudes of V2493 Cyg were then calculated by performing differential photometry on the set of images for each night interpolated to a seeing of 1″.5 (median seeing during our observations).

Previously, Semkov et al. (2010) have listed 7 stars as local standardsAll-Sky Automated Survey for Supernovae near V2493 Cyg. Out of them, we have selected 4 stars (2 stars in the NIR wavelengths) for our analysis, which are located in the common field of view of the detectors used. We have also observed the Landolt standard field (Landolt 1992) SA 98 (α_{J2000}: $06^h52^m14^s$, δ_{J2000}: $-00°18'59''$) on the night of 2019 November 4. This is done to calculate the present V, R_C, and I_C magnitudes of the selected local standards. We have also checked the long-term behavior of the selected local standards in ASAS-SN[10] survey to verify the stability of magnitudes of our selected local standards. The calibration equations derived from the Landolt standard stars by the least-squares linear regression are as follows:

$$V = v + (2.46 \pm 0.01) + (0.04 \pm 0.01) \times (v - i_c) + 0.19 \pm 0.01 \times X_V, \quad (1)$$

$$R_C = r_c + (2.06 \pm 0.01) + (0.05 \pm 0.01) \times (v - r_c) + 0.17 \pm 0.01 \times X_R, \quad (2)$$

$$I_C = i_c + (2.59 \pm 0.01) + (-0.03 \pm 0.01) \times (v - i_c) + 0.11 \pm 0.01 \times X_I, \quad (3)$$

where v, r_c, and i_c are the instrumental magnitudes, and V, R_C, and I_C are the standard magnitudes. X is the airmass term in the corresponding filters. In the NIR wavelengths, we have calibrated the local standard stars using the color transformation equations provided by Ninan et al. (2014). The rest of the procedures to calibrate V2493 Cyg is similar to what has been described in Ghosh et al. (2022a). Table 2 lists the coordinates and V, R_C, I_C, J, H, and K_S magnitudes of the local standard stars used in the present study. Table 3 provides the calibrated V, R_C, I_C, J, H, and K_S magnitudes of V2493 Cyg at 54 epochs starting from 2013 September up to 2019 December.

2.2. Archival Data

We have obtained B, V, R, and I photometric data provided by Semkov et al. (2010) in their study. Photometric data in the above bands are also downloaded from the archive of American Association for the Variable Star Observers (AAVSO).[11]

We have also acquired the photometric data provided by the PTF in their g and R bands.[12] The details of PTF survey are provided in Law et al. (2009).

Multiepoch photometric data of V2493 Cyg are also available in the Zwicky Transient Facility (ZTF) archive. We have downloaded the ZTF Data Release 6 zg- and zr-band data from the NASA/IPAC Infrared Science Archive.[13] The details of the ZTF are available in Bellm et al. (2018).

Archival mid-infrared (MIR) data in W1 (3.4 μm) and W2 (4.6 μm) channels from the Near-Earth Object Wide-field Infrared Survey Explorer (NEOWISE) survey are obtained from the NASA/IPAC Infrared Science archive.[14] The details of the NEOWISE survey are available at Mainzer et al. (2014).

2.3. Spectroscopic Data

2.3.1. Medium-resolution Single-order Optical Spectroscopy

V2493 Cyg is monitored spectroscopically starting from 2015 May 17 to 2021 June 14 at 28 different epochs using the HFOSC. HFOSC provides a medium-resolution spectra with $R \sim 2000$ with 1″ slit from $\sim$4000 to 9000 Å using grisms Gr7 and Gr8.

Standard IRAF[15] tasks are used for the spectroscopic data reduction. The task APALL is used to extract the spectrum in one-dimensional format. The extracted spectrum is then wavelength calibrated using the task IDENTIFY with the help of calibration lamps (FeAr and FeNe) taken immediately after the source spectrum. We have followed this with the task CONTINUUM to continuum normalize our spectra. We have used this normalized spectra to measure the equivalent widths (W_λ) of important spectral lines by using the SPLOT package of IRAF. Three independent measurements of W_λ per line are made, and the median value of those measurements is taken as the final W_λ of that particular line.

2.3.2. Medium-resolution Echelle Spectroscopy

We have obtained medium-resolution echelle spectrum of V2493 Cyg on 2019 April 28 by using the Medium

---

Table 1
Log of Photometric and Spectroscopic Observations

Telescope/Instrument	Date	JD	Filters/Grisms	Exposure(s) = Int. Time (s) × No. of Frames (f) / Int. Time (s) × No. of Frames (f) × No. of Dither Positions (d)[a]
2.0 m HCT TIRSPEC	2013 Sep 27	2,456,563	J, H, K_S	20 s × 3 f × 5 d, 15 s × 3 f × 5 d, 20 s × 3 f × 5 d
"	2013 Nov 14	2,456,611	H, K_S	15 s × 3 f × 5 d, 20 s × 3 f × 5 d
"	2013 Nov 30	2,456,627	J, H, K_S	20 s × 3 f × 5 d, 15 s × 3 f × 5 d, 20 s × 3 f × 5 d
"	2013 Dec 20	2,456,647	K_S	20 s × 3 f × 5 d
"	2014 Mar 7	2,456,725	H,K	100 s × 6 f, 100 s × 6 f
"	2014 Mar 25	2,456,742	J, H, K_S	20 s × 3 f × 5 d, 15 s × 3 f × 5 d, 20 s × 3 f × 5 d
"	2014 May 04	2,456,782	J, H, K_S	20 s × 3 f × 5 d, 15 s × 3 f × 5 d, 20 s × 3 f × 5 d
"	2014 May 29	2,456,807	J, H	15 s × 3 f × 5 d, 20 s × 3 f × 5 d
"	2014 Jun 4	2,456,813	K	100 s × 6 f
"	2014 Jun 5	2,456,814	J, H, K_S	20 s × 3 f × 5 d, 15 s × 3 f × 5 d, 20 s × 3 f × 5 d
"	2014 Jul 2	2,456,841	J,H,K,J, H, K_S	100 s × 6 f, 100 s × 6 f, 100 s × 6 f, 20 s × 3 f × 5 d, 15 s × 3 f × 5 d, 20 s × 3 f × 5 d
"	2014 Jul 3	2,456,842	J, H, K_S	20 s × 3 f × 5 d, 15 s × 3 f × 5 d, 20 s × 3 f × 5 d
"	2014 Aug 24	2,456,894	H,K,J	100 s × 6 f, 100 s × 6 f, 20 s × 3 f × 5 d
"	2014 Aug 25	2,456,895	Y,J,J, H, K_S	100 s × 6 f, 100 s × 6 f, 20 s × 3 f × 5 d, 15 s × 3 f × 5 d, 20 s × 3 f × 5 d
"	2014 Sep 25	2,456,926	K,J, H, K_S	100 s × 6 f, 20 s × 3 f × 5 d, 15 s × 3 f × 5 d, 20 s × 3 f × 5 d
"	2014 Sep 26	2,456,927	Y,J,H,K	100 s × 6 f, 100 s × 6 f, 100 s × 6 f, 100 s × 3 f × 2 d
"	2014 Oct 26	2,456,957	J, H, K_S	20 s × 3 f × 5 d, 15 s × 3 f × 5 d, 20 s × 3 f × 5 d
"	2014 Nov 21	2,456,983	Y,J, J, H, K_S	100 s × 6 f, 100 s × 6 f, 20 s × 3 f × 5 d, 15 s × 3 f × 5 d, 20 s × 3 f × 5 d
"	2014 Nov 22	2,456,984	Y,J,H,K	100 s × 6 f, 100 s × 6 f, 100 s × 6 f, 100 s × 6 f
"	2014 Nov 28	2,456,990	J, H, K_S	20 s × 3 f × 5 d, 15 s × 3 f × 5 d, 20 s × 3 f × 5 d
"	2014 Dec 25	2,457,017	J	20 s × 3 f × 5 d
"	2015 Feb 12	2,457,066	J, K_S	20 s × 3 f × 5 d, 15 s × 3 f × 5 d, 20 s × 3 f × 5 d
"	2015 Apr 14	2,457,127	K_S	20 s × 3 f × 5 d
"	2015 Apr 27	2,457,141	Y,J,H,K	100 s × 6 f, 100 s × 6 f, 100 s × 6 f, 100 s × 6 f
TIRSPEC+HFOSC	2015 May 16	2,457,159	V, R, J, H, K_S	60 s × 3 f, 30 s × 3 f, 20 s × 3 f × 5 d, 15 s × 3 f × 5 d, 20 s × 3 f × 5 d
"	2015 May 26	2,457,170	Y,J,H,K	100 s × 6 f, 100 s × 6 f, 100 s × 6 f, 100 s × 6 f
HFOSC	2015 Jun 10	2,457,184	V, R, I_c	60 s × 3 f, 30 s × 3 f, 30 s × 3 f
TIRSPEC	2015 Jun 23	2,457,197	J,H,K	100 s × 6 f, 100 s × 6 f, 100 s × 6 f
"	2015 Jul 27	2,457,231	J,H,K J, H, K_S	100 s × 6 f, 100 s × 6 f, 100 s × 6 f, 20 s × 3 f × 5 d, 15 s × 3 f × 5 d, 20 s × 3 f × 5 d
"	2015 Aug 17	2,457,252	Y,J,H,K,J, H, K_S	100 s × 6 f , 100 s × 6 f, 100 s × 6 f, 100 s × 6 f, 20 s × 3 f × 5 d, 15 s × 3 f × 5 d, 20 s × 3 f × 5 d
"	2015 Oct 13	2,457,309	Y,J,J, H, K_S	100 s × 6 f , 100 s × 6 f, 20 s × 3 f × 5 d, 15 s × 3 f × 5 d, 20 s × 3 f × 5 d
HFOSC	2015 May 17	2,457,160	Gr7, Gr8	1800 s , 1800 s
"	2015 May 26	2,457,169	Gr8	1200 s
"	2015 Jun 10	2,457,184	Gr7, Gr8	1200 s , 1200 s
"	2015 Aug 18	2,457,253	V, R, Gr7, Gr8	60 s × 3 f, 30 s × 3 f, 1200 s, 1200 s
"	2015 Sep 27	2,457,293	V, R, Gr7, Gr8	60 s × 3 f, 30 s × 3 f, 1200 s, 1200 s
"	2015 Oct 12	2,457,308	V, R, Gr7, Gr8	60 s × 3 f, 30 s × 3 f, 1200 s, 1200 s
1.3 m DFOT ANDOR 512 × 512	2015 Oct 16	2,457,312	V, R_c, I_c	60 s × 3 f, 30 s × 3 f, 30 s × 3 f
"	2015 Nov 2	2,457,329	R_c, I_c	30 s × 3 f, 30 s × 3 f
HFOSC	2015 Nov 10	2,457,337	V, R, Gr7	60 s × 3 f, 30 s × 3 f, 1200 s
ANDOR 512 × 512	2015 Nov 18	2,457,345	V, R_c, I_c	60 s × 3 f, 30 s × 3 f, 30 s × 3 f
"	2016 Jan 1	2,457,390	V, R_c, I_c	60 s × 3f, 30 s × 3f, 30 s × 3 f
HFOSC	2016 Jan 20	2,457,409	Gr7, Gr8	1200 s,1200 s
"	2016 Mar 3	2,457,451	V, R	60 s × 3 f, 30 s × 3 f
"	2016 Mar 15	2,457,463	V, R, Gr7, Gr8	60 s × 3 f, 30 s × 3 f, 900 s, 900 s
"	2016 Jun 17	2,457,557	V, R, Gr7, Gr8	60 s × 3 f, 30 s × 3 f, 1200 s,1200 s
"	2016 Jul 24	2,457,594	V, R, Gr7, Gr8	60 s × 3 f, 30 s × 3 f, 1800 s,1200 s
"	2016 Sep 26	2,457,658	V, R, Gr7, Gr8	60 s × 3 f, 30 s × 3 f, 1800 s,1800 s
"	2016 Oct 5	2,457,667	V, R, Gr8	60 s × 3 f, 30 s × 3 f, 700 s
ANDOR 512 × 512	2016 Oct 08	2,457,670	V, R_c, I_c	60 s × 3 f, 30 s × 3 f, 30 s × 3 f
HFOSC	2016 Oct 13	2,457,675	V, R, I_c, Gr7, Gr8	60 s × 3 f, 30 s × 3 f, 30 s × 3 f, 1800 s, 1200 s
ANDOR 512 × 512	2016 Nov 15	2,457,708	V, R_c, I_c	60 s × 3 f, 30 s × 3 f, 30 s × 3 f
HFOSC	2016 Nov 17	2,457,710	V, R, I_c, Gr7, Gr8	60 s × 3 f, 30 s × 3 f, 30 s × 3 f, 1200 s, 1200 s
"	2016 Dec 04	2,457,727	V, R, I_c, Gr7, Gr8	60 s × 3 f, 30 s × 3 f, 30 s × 3 f, 1200 s, 1200 s
"	2016 Dec 08	2,457,731	H, K, Gr7, Gr8	100 s × 6 f, 100 s × 6 f, 1800 s, 1800 s

Table 1
(Continued)

Telescope/Instrument	Date	JD	Filters/Grisms	Exposure(s) = Int. Time (s) × No. of Frames (f) / Int. Time (s) × No. of Frames (f) × No. of Dither Positions (d)[a]
"	2017 Apr 25	2,457,869	Gr7, Gr8	1800 s , 1800 s
"	2017 Apr 28	2,457,872	Gr7	1800 s
TIRSPEC	2017 Jul 2	2,457,937	Y,J,H,K	100 s × 6 f , 100 s × 6 f, 100 s × 6 f, 100 × 3 f
HFOSC	2017 Jul 3	2,457,938	Gr8	1800 s
TIRSPEC	2017 Aug 20	2,457,983	J, H, K_S	20 s × 3 f × 5 d, 15 s × 3 f × 5 d, 20 s × 3 f × 5 d
HFOSC	2017 Aug 22	2,457,985	Gr8	1800 s
TIRSPEC	2017 Sep 14	2,458,011	Y,J,H,K, J, H, K_S	100 s × 6 f, 100 s × 6 f, 100 s × 6 f, 100 s × 6 f, 20 s × 3 f × 5 d, 15 s × 3 f × 5 d, 20 s × 3 f × 5 d
HFOSC	2017 Sep 17	2,458,014	Gr7, Gr8	1800 s, 1800 s
ANDOR 512 × 512	2017 Oct 8	2,458,035	V, R_c, I_c	60 s × 3 f, 30 s × 3 f, 30 s × 3 f
1.3 m DFOT ANDOR 2k × 2k	2017 Oct 13	2,458,040	V, R_c, I_c	60 s × 3 f, 30 s × 3 f, 30 s × 3 f
"	2017 Nov 11	2,458,069	V, R_c, I_c	60 s × 3 f, 30 s × 3 f, 30 s × 3 f
"	2017 Dec 10	2,458,098	V, R_c, I_c	60 s × 3 f, 30 s × 3 f, 30 s × 3 f
HFOSC	2018 Aug 13	2,458,344	V, R, I_c, Gr7, Gr8	60 s × 3 f, 30 s × 3 f, 30 s × 3 f, 1800 s, 2700 s
ANDOR 2k × 2k	2018 Oct 06	2,458,398	V, R_c, I_c	60 s × 3 f, 30 s × 3 f, 30 s × 3 f
"	2018 Oct 18	2,458,410	V, R_c, I_c	60 s × 3 f, 30 s × 3 f, 30 s × 3 f
HFOSC	2018 Nov 6	2,458,429	Gr7, Gr8	1200 s, 1200 s
TIRSPEC	2018 Nov 7	2,458,429	Y,J,H,K	100 s × 6 f, 100 s × 6 f, 100 s × 6 f, 100 s × 6 f
HFOSC	2018 Nov 21	2,458,444	Gr7, Gr8	1800 s, 1200 s
ANDOR 512 × 512	2018 Nov 25	2,458,448	V, R_c, I_c	60 s × 3 f, 30 s × 3 f, 30 × 3f
ANDOR 2k × 2k	2018 Nov 26	2,458,449	V, R_c, I_c	60 s × 3 f, 30 s × 3 f, 30 × 3f
ANDOR 2k × 2k	2018 Dec 3	2,458,456	V, R_c, I_c	60 × 3, 30 × 3, 30 × 3 60 s × 3 f, 30 × 3 f, 30 × 3f
HFOSC	2018 Dec 12	2,458,465	Gr7, Gr8	1500 s, 900 s
ANDOR 512 × 512	2018 Dec 20	2,458,473	V, R_c, I_c	60 s × 3 f, 30 s × 3 f, 30 × f
TIRSPEC	2018 Dec 24	2,458,477	J, H, K_S	20 s × 3 f × 5 d, 15 s × 3 f × 5 d, 20 s × 3 f × 5 d
HFOSC	2018 Dec 25	2,458,478	Gr7, Gr8	1500 s, 900 s
2.4 m TNT MRES	2019 Apr 28	2,458,602	Echelle spectra	3600 s
ANDOR 512 × 512	2019 May 20	2,458,624	V, R_c, I_c	60 × 3, 30 × 3, 30 × 3
TIRSPEC	2019 Jun 14	2,458,649	J, H, K_S	20 s × 3 f × 5 d, 15 s × 3 f × 5 d, 20 s × 3 f × 5 d
"	2019 Oct 12	2,458,769	J, H, K_S	20 s × 3 f × 5 d, 15 s × 3 f × 5 d, 20 s × 3 f × 5 d
HFOSC	2019 Oct 28	2,458,785	Gr8	1800 s
ANDOR 2k × 2k	2019 Nov 4	2,458,792	V, R_c, I_c	60 s × 3 f, 30 s × 3 f, 30 s × 3 f
"	2019 Nov 5	2,458,793	R_c, I_c	30 s × 3 f, 30 s × 3 f
"	2019 Nov 6	2,458,794	V, R_c, I_c	60 s × 3 f, 30 s × 3 f, 30 s × 3 f
"	2019 Nov 25	2,458,813	V, R_c, I_c	60 s × 3 f, 30 s × 3 f, 30 s × 3 f
"	2019 Nov 29	2,458,817	V, R_c, I_c	60 s × 3 f, 30 s × 3 f, 30 s × 3 f
"	2019 Dec 8	2,458,826	V, r_c, I_c	60 s × 3 f, 30 s × 3 f, 30 s × 3 f
"	2019 Dec 16	2,458,834	V, R_c, I_c	60 s × 3 f, 30 s × 3 f, 30 s × 3 f
"	2019 Dec 30	2,458,848	V, R_c, I_c	60 s × 3 f, 30 s × 3 f, 30 s × 3 f
3.6 m DOT TANSPEC	2020 Oct 25	2,459,148	Cross-dispersed spectra	120 s × 5 f
"	2020 Nov 10	2,459,164	Cross-dispersed spectra	120 s × 5 f
HFOSC	2021 Jun 14	2,459,380	Gr7, Gr8	1800 s, 1800 s

Note.
[a] For the NIR photometric observations.

Table 2
Coordinates and Magnitudes of the Local Standard Stars

Names	α_{2000} (degrees)	δ_{2000} (degrees)	$V \pm \sigma$ (mag)	$R_C \pm \sigma$ (mag)	$I_C \pm \sigma$ (mag)	$J \pm \sigma$ (mag)	$H \pm \sigma$ (mag)	$K_S \pm \sigma$ (mag)
2MASS J20583004+4352257	314.625108	+43.874258	15.02 ± 0.01	14.10 ± 0.01	13.20 ± 0.01	⋯	⋯	⋯
2MASS J20583004+4352257	314.631458	+43.874539	15.45 ± 0.01	14.79 ± 0.01	14.15 ± 0.01	13.47 ± 0.01	12.97 ± 0.01	12.87 ± 0.01
USNO-B1.0 1338-00391522	314.610204	+43.873175	15.87 ± 0.01	14.90 ± 0.01	13.92 ± 0.01	12.99 ± 0.01	12.40 ± 0.01	12.13 ± 0.01
2MASS J20581249+4352347	314.552492	+43.876633	15.92 ± 0.01	15.12 ± 0.01	14.48 ± 0.01	13.70 ± 0.01	13.10 ± 0.01	12.96 ± 0.01

Resolution Echelle Spectrograph (MRES), which is mounted on the 2.4 m Thai National Telescope (TNT) located at Thai National Observatory. MRES has wavelength coverage from 3900 to 8800 Å, and it provides a spectral resolution of $R \sim 16{,}000$–$19{,}000$. Details about the MRES instrument can be found in Yadav et al. (2022). The lunar illumination during our observation date was ∼33%, and the sky was hazy due to forest fires resulting in low signal-to-noise ratio (S/N). We

Table 3
Photometric Magnitudes of V2493 Cyg in Different Filters Using the Present Observations.

Julian Day	V	R	I_C	J	H	K_S
2456563	⋯	⋯	⋯	9.35 ± 0.01	8.37 ± 0.01	8.04 ± 0.01
2456611	⋯	⋯	⋯	⋯	8.52 ± 0.01	7.97 ± 0.01
2456627	⋯	⋯	⋯	9.26 ± 0.01	8.45 ± 0.01	7.94 ± 0.01
2456647	⋯	⋯	⋯	⋯	⋯	7.94 ± 0.01
2456742	⋯	⋯	⋯	9.34 ± 0.01	8.50 ± 0.01	8.03 ± 0.01
2456782	⋯	⋯	⋯	9.36 ± 0.01	8.57 ± 0.01	7.96 ± 0.01
2456807	⋯	⋯	⋯	9.33 ± 0.01	8.49 ± 0.01	⋯
2456814	⋯	⋯	⋯	9.36 ± 0.01	8.52 ± 0.01	8.13 ± 0.02
2456841	⋯	⋯	⋯	9.36 ± 0.01	8.49 ± 0.01	7.96 ± 0.01
2456842	⋯	⋯	⋯	9.32 ± 0.01	8.45 ± 0.01	7.96 ± 0.01
2456894	⋯	⋯	⋯	9.30 ± 0.01	⋯	⋯
2456895	⋯	⋯	⋯	9.31 ± 0.01	8.48 ± 0.01	7.94 ± 0.01
2456926	⋯	⋯	⋯	9.24 ± 0.01	8.43 ± 0.01	7.86 ± 0.01
2456957	⋯	⋯	⋯	9.24 ± 0.01	8.30 ± 0.01	7.80 ± 0.01
2456983	⋯	⋯	⋯	9.22 ± 0.01	8.45 ± 0.01	7.89 ± 0.01
2456990	⋯	⋯	⋯	9.31 ± 0.01	8.48 ± 0.01	7.92 ± 0.01
2457017	⋯	⋯	⋯	9.34 ± 0.01	⋯	⋯
2457066	⋯	⋯	⋯	9.23 ± 0.01	⋯	7.89 ± 0.02
2457127	⋯	⋯	⋯	⋯	⋯	7.89 ± 0.02
2457159	13.43 ± 0.01	12.25 ± 0.01	⋯	9.29 ± 0.01	8.42 ± 0.01	7.75 ± 0.01
2457184	13.41 ± 0.01	12.29 ± 0.01	11.10 ± 0.01	⋯	⋯	⋯
2457231	⋯	—	⋯	9.39 ± 0.01	8.35 ± 0.01	7.81 ± 0.01
2457252	⋯	—	⋯	9.33 ± 0.01	8.40 ± 0.01	7.87 ± 0.01
2457253	13.29 ± 0.03	12.16 ± 0.01	⋯	⋯	⋯	⋯
2457293	13.39 ± 0.01	12.34 ± 0.01	⋯	⋯	⋯	⋯
2457308	13.42 ± 0.02	⋯	—	⋯	⋯	⋯
2457309	⋯	—	⋯	9.25 ± 0.01	8.48 ± 0.01	7.86 ± 0.01
2457312	13.50 ± 0.01	12.45 ± 0.01	11.44 ± 0.02	⋯	⋯	⋯
2457329	⋯	12.29 ± 0.01	11.17 ± 0.01	⋯	⋯	⋯
2457337	13.36 ± 0.02	12.22 ± 0.02	⋯	⋯	⋯	⋯
2457345	13.53 ± 0.01	12.34 ± 0.01	11.13 ± 0.01	⋯	⋯	⋯
2457390	13.57 ± 0.01	12.39 ± 0.01	11.12 ± 0.01	⋯	⋯	⋯
2457451	13.34 ± 0.01	12.22 ± 0.03	⋯	⋯	⋯	⋯
2457463	13.40 ± 0.01	12.34 ± 0.01	11.15 ± 0.01	⋯	⋯	⋯
2457557	13.25 ± 0.01	12.24 ± 0.01	⋯	⋯	⋯	⋯
2457594	13.42 ± 0.01	12.27 ± 0.01	⋯	⋯	⋯	⋯
2457658	13.31 ± 0.01	12.25 ± 0.01	⋯	⋯	⋯	⋯
2457667	13.43 ± 0.01	12.23 ± 0.01	⋯	⋯	⋯	⋯
2457660	13.66 ± 0.01	12.51 ± 0.01	11.27 ± 0.01	⋯	⋯	⋯
2457670	13.61 ± 0.01	12.45 ± 0.01	11.24 ± 0.01	⋯	⋯	⋯
2457675	13.55 ± 0.01	12.37 ± 0.01	11.15 ± 0.01	⋯	⋯	⋯
2457708	13.62 ± 0.01	12.49 ± 0.01	11.25 ± 0.01	⋯	⋯	⋯
2457710	13.63 ± 0.01	12.37 ± 0.01	11.18 ± 0.01	⋯	⋯	⋯
2457727	13.41 ± 0.01	12.27 ± 0.01	11.12 ± 0.01	⋯	⋯	⋯
2457976	13.65 ± 0.02	12.40 ± 0.01	11.16 ± 0.01	⋯	⋯	⋯
2457986	⋯	⋯	⋯	9.24 ± 0.01	8.42 ± 0.01	7.74 ± 0.01
2458011	⋯	⋯	⋯	9.22 ± 0.01	8.46 ± 0.01	7.80 ± 0.01
2458344	13.73 ± 0.01	12.77 ± 0.01	11.14 ± 0.01	⋯	⋯	⋯
2458448	13.57 ± 0.01	12.26 ± 0.01	11.10 ± 0.01	⋯	⋯	⋯
2458473	13.38 ± 0.02	12.28 ± 0.01	11.15 ± 0.01	⋯	⋯	⋯
2458477	⋯	⋯	⋯	9.16 ± 0.01	8.42 ± 0.004	7.76 ± 0.01
2458624	13.73 ± 0.01	12.49 ± 0.01	11.23 ± 0.01	⋯	⋯	⋯
2458649	⋯	⋯	⋯	9.26 ± 0.01	8.37 ± 0.01	7.63 ± 0.02
2458040	13.62 ± 0.01	12.46 ± 0.01	11.19 ± 0.01	⋯	⋯	⋯
2458069	13.58 ± 0.01	12.43 ± 0.01	11.18 ± 0.01	⋯	⋯	⋯
2458098	13.54 ± 0.01	12.36 ± 0.01	11.12 ± 0.01	⋯	⋯	⋯
2458398	13.48 ± 0.01	12.35 ± 0.01	11.09 ± 0.01	⋯	⋯	⋯
2458410	13.49 ± 0.01	12.38 ± 0.01	11.09 ± 0.01	⋯	⋯	⋯
2458449	13.54 ± 0.01	12.39 ± 0.01	11.12 ± 0.01	⋯	⋯	⋯
2458456	13.48 ± 0.01	12.34 ± 0.01	11.08 ± 0.01	⋯	⋯	⋯
2458769	⋯	⋯	—	9.37 ± 0.01	8.58 ± 0.01	7.95 ± 0.02
2458792	13.76 ± 0.01	12.56 ± 0.01	11.23 ± 0.01	⋯	⋯	⋯
2458793	⋯	12.56 ± 0.01	11.22 ± 0.01	⋯	⋯	⋯
2458794	13.81 ± 0.01	12.61 ± 0.01	11.27 ± 0.01	⋯	⋯	⋯

Table 3
(Continued)

Julian Day	V	R	I_C	J	H	K_S
2458813	13.81 ± 0.01	12.59 ± 0.01	11.27 ± 0.01	⋯	⋯	⋯
2458817	13.70 ± 0.01	12.48 ± 0.01	11.17 ± 0.01	⋯	⋯	⋯
2458826	13.71 ± 0.01	12.50 ± 0.01	11.18 ± 0.01	⋯	⋯	⋯
2458834	13.92 ± 0.01	12.76 ± 0.01	11.43 ± 0.01	⋯	⋯	⋯
2458848	13.74 ± 0.01	12.53 ± 0.01	11.21 ± 0.01	⋯	⋯	⋯

can only use the spectrum covering the wavelength range of 3900 to 6600 Å for our present analysis. A wavelength beyond this range is dominated by multiple telluric lines and bands and hence is not used for the analysis.

We have used the standard calibration frames, e.g., bias, flat, and Th-Ar lamp, for image cleaning and wavelength calibration. The spectrum is extracted using the ECHELLE module of the IRAF package. The procedure to calibrate the wavelength and normalize the spectrum is similar to that which has been described in Section 2.3.1.

2.3.3. NIR Spectroscopy

We have spectroscopically monitored V2493 Cyg in the NIR wavelengths starting from 2014 March 07 until 2020 November 11 using the TIRSPEC mounted on 2 m HCT and TIFR-ARIES Near Infrared Spectrograph (TANSPEC; Ojha et al. 2018; Sharma et al. 2022) mounted on 3.6 m Devasthal Optical Telescope (DOT). TIRSPEC provides a wavelength coverage from 1 to 2.5 μm at a spectral resolution of ∼1200. The details about the instrument are provided in Ninan et al. (2014). The TIRSPEC spectroscopic data are processed using the TIRSPEC pipeline.[16] The sky conditions were poor on the nights of 2017 September 14 and 2018 November 7 leading to poor S/N in the extracted spectra. The output extracted spectrum obtained is continuum normalized using the CONTINUUM task of IRAF.

We have also obtained the NIR spectra of V2493 Cyg using the TANSPEC with its 1″0 slit providing a R∼1500 on the nights of 2020 October 25 and 2020 November 11. The spectra are obtained following the technique that is described in detail in Ghosh et al. (2022a). The obtained spectra are then wavelength calibrated by using the recently developed TANSPEC data reduction pipeline[17] (Ghosh et al. 2022b). The telluric correction to the spectra is done in a similar manner as described in Ghosh et al. (2022a). The resulting spectra are then continuum normalized using the Python SPECUTILS module[18] (Earl et al. 2021).

In summary, we have monitored V2493 Cyg spectroscopically at 50 epochs with HFOSC (28), MRES (1), TIRSPEC (19), and TANSPEC (2) starting from 2014 July until 2021 June. Table 1 contains the complete log of spectroscopic observations.

3. Results and Analysis

3.1. Light Curve

The top panel of Figure 2 shows the light curve (LC) of V2493 Cyg in optical B, V, R_C, and I_C, PTF g' and R, ZTF zg,

and zr, NIR J, H, and K_S and NEOWISE MIR W1 and W2 bands. The data in the V, R, and I_C bands have the longest coverage. We have combined our V-, R_C-, I_C-, J-, H-, and K_s-band data[19] with that of the archival data from AAVSO and the previously published data taken from Semkov et al. (2010, 2021), Miller et al. (2011), and Kóspál et al. (2016). The photometric monitoring timescales of the different surveys both in optical and NIR bands of V2493 Cyg begin with the Two Micron All Sky Survey (2MASS) observations on 2000 June 10 (JD = 2451706). V2493 Cyg was then observed in NIR bands during its 2010 outburst, by Miller et al. (2011) and Leoni et al. (2010), as shown in Figure 3. Our monitoring period is denoted by the orange horizontal bars. We have monitored V2493 Cyg photometrically both in optical and NIR wave bands.

Baek et al. (2015) have studied the photometric evolution of V2493 Cyg from 2010 September to 2013 May. During this period, V2493 Cyg transitioned to its first outburst state to an intermediate quiescent stage and finally to its second outburst state. They have subsequently divided this period into 5 phases based on the LC evolution. We call our optical photometric monitoring period, which is carried out between 2015 October 16 and 2021 December 4, phase (6), which is actually a period after the peak of second outburst. The middle panel of Figure 2 shows the LC of V2493 Cyg during our monitoring period. During phase (6), in the period between 2015 October 16 and 2019 December 30,[20] the V-band brightness of V2493 Cyg dimmed at an average rate of ∼2.3 mmag/month with a drop by ∼0.6 mag from its peak outburst V-band magnitude in August 2010. Since the dimming rate is too small, we can call phase (6) a *long plateau* phase also. Such a long plateau phase, which is also observed in other bona fide FUor sources like FU Ori, etc., is attributed to the time required to deplete the inner disk completely (see Audard et al. 2014). We note that the individual Wide-field Infrared Survey Explorer (WISE) measurements for a given JD showed considerable scatter. We have therefore used the median WISE magnitudes for a given JD in our MIR analysis. We have taken the standard deviation of the magnitude variations within a day as a conservative limit of measurement error. In the same duration, the source seems to brighten-up by ∼0.7 mag and ∼0.4 mag in MIR W1 and W2 bands, respectively, with an average rise rate of ∼94 ± 18 and 62 ± 7 mmag yr^{-1}.

3.2. Color Evolution

The bottom panel of Figure 2 shows the complete evolution of $(V - I_C)$ and $(V - R_C)$ colors coded onto the V-band magnitude of V2493 Cyg from 2015 October 16 to 2019
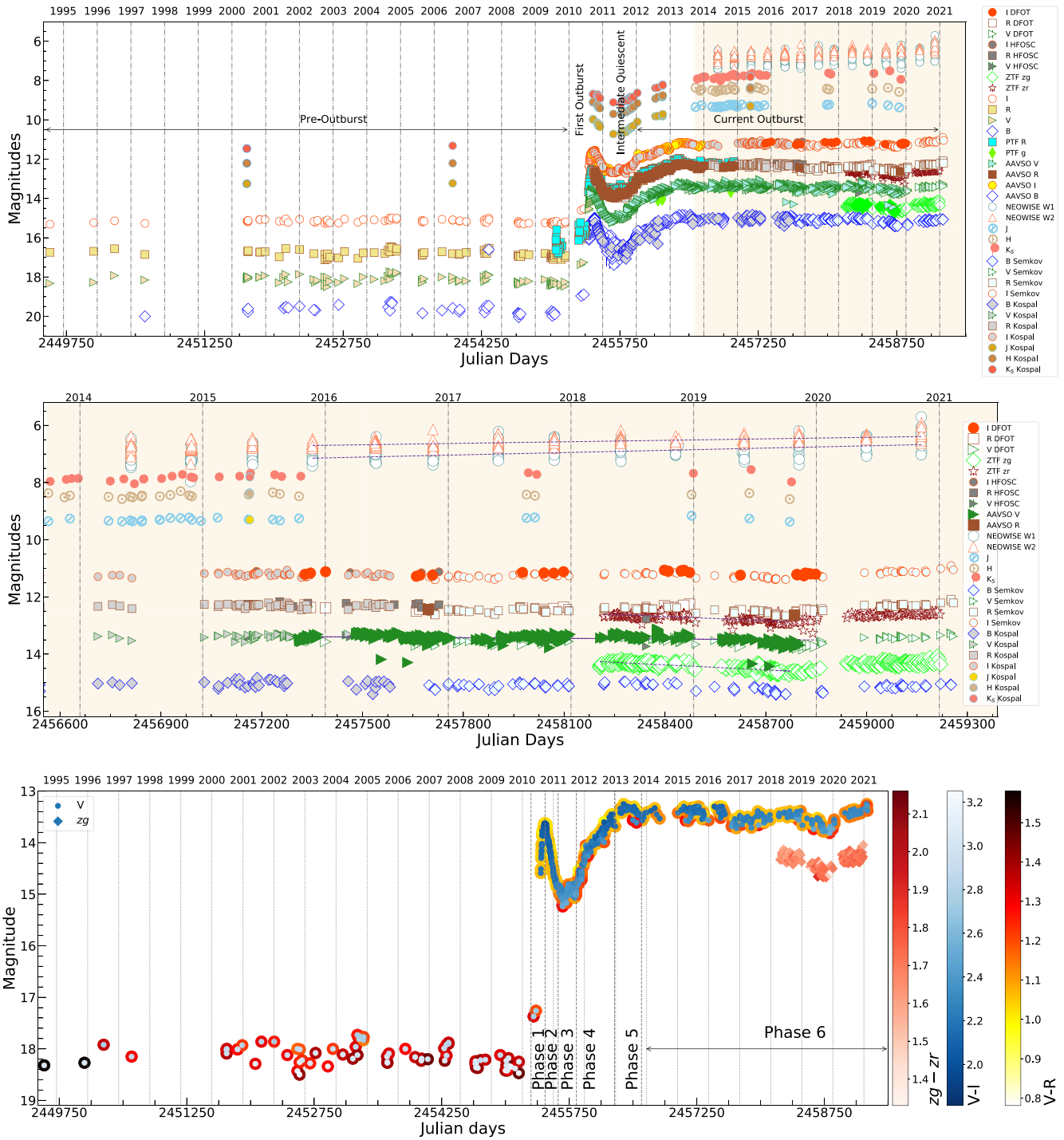
---

[16] http://indiajoe.github.io/TIRSPEC/Pipeline/
[17] https://github.com/astrosupriyo/pyTANSPEC
[18] https://specutils.readthedocs.io/en/stable/

[19] Optical photometric data obtained with the 1.3 m DFOT telescope and NIR photometric data from 2 m HCT telescope.
[20] This time period coincides with our monitoring of V2493 Cyg with 1.3 m DFOT.

Figure 2. Top panel: light curve of V2493 Cyg in Johnson–Cousins B, V, R_C, and I_C, ZTF zg and zr, PTF g', and R, J, H, and K_S, and NEOWISE W1 and W2 bands showing pre-outburst, first outburst, intermediate quiescent phase, and the current outburst phase. The shaded region is our monitoring period. Middle panel shows the zoomed-in LC of V2493 Cyg, which covers our monitoring period corresponding to the time period between 2013 September 9 and 2021 January 4. We call our monitoring period phase (6). Bottom panel: V-band LC of V2493 Cyg coded with that of $V - R$ and $V - I_C$ colors. The $V - R$ color is depicted at the outer ring (annulus), while the color in the center depicts $V - I_C$ color. The diamonds represent the zg-band LC coded with $zg - zr$ color. We find that all the colors are slowly becoming redder. The different phases, starting from phase (1) to phase (5), are adopted from the study of Baek et al. (2015).

December 30, which is within phase (6) defined earlier. Both the $(V - R_C)$ and $(V - I_C)$ colors have consistently become redder in phase (6), implying the presence of a cooler flux than what was present during the previous phases. During phase (5), V2493 Cyg showed a weak bluer trend with small-scale fluctuations in its color (Baek et al. 2015). Therefore, the present evolution possibly points toward a different physical

process occurring in the V2493 Cyg as compared to the previous phases. The $V - R_C$ and $V - I_C$ colors have become redder by 0.14 and 0.32 mag, respectively, during phase (6). The color evolution of V2493 Cyg is similar to that of V899 Mon, in a sense that its transition fluxes are redder compared to the outburst stages, therefore implying that the outburst flux possibly has emerged from the circumstellar disk
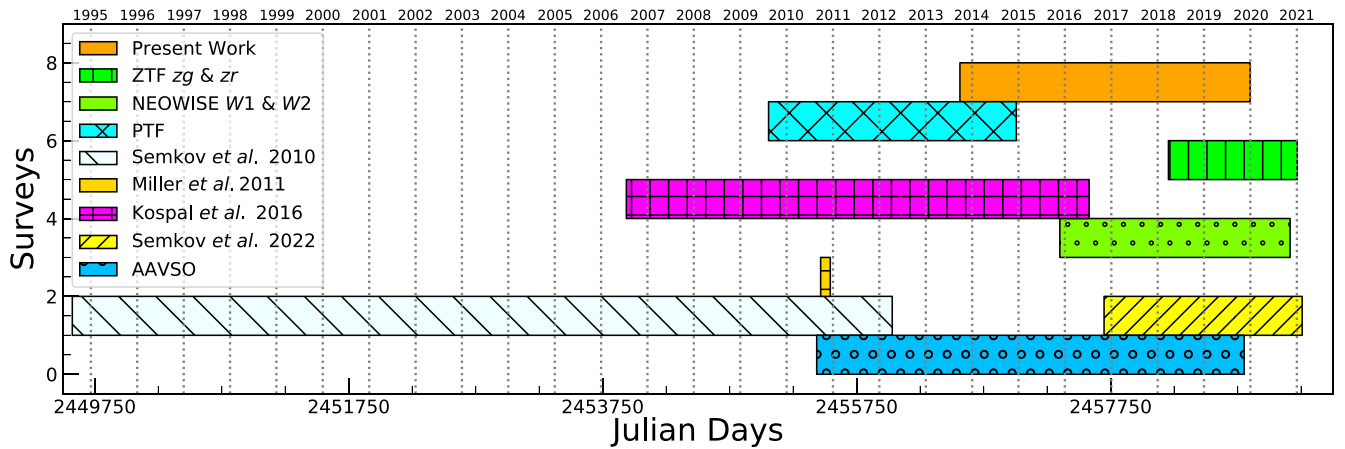
Figure 3. Timescales of the different studies and surveys at optical and NIR wave bands with which the evolution of V2493 Cyg was monitored. Our monitoring program is denoted by the orange horizontal bar, and it includes monitoring in both optical and NIR wave bands. Semkov et al. (2010, 2021) monitored V2493 Cyg extensively in optical wave bands as shown. The NIR monitoring was primarily carried out by Miller et al. (2011) and Kóspál et al. (2016), which covered both the 2010 and 2012 outburst.

(Ninan et al. 2015). Semkov et al. (2021) have also noted this color evolution in their monitoring during the phase (6) period. The reddening of the optical colors can be a result of gradual decline in accretion rate in V2493 Cyg such that the central PMS star is exiting the maximum phase of the FUor outburst (Semkov et al. 2021). Alternatively, the reddening of the optical colors can also be possibly explained due to the expansion of the emitting region around the star. This expansion of the emitting area is possibly a result of an ionization front expanding outwards (Kóspál et al. 2016). The color evolution of V2493 Cyg can be further analyzed based on the theoretical model developed by Liu et al. (2022). According to their model, the PMS stars accreting in the "FU Ori" regime occupy a certain locus in the color–magnitude diagram (CMD) plane as compared to the stars still accreting via magnetospheric regime. They introduced a parameter η, which is the ratio of total H- and K-band viscous disk flux to that of the PMS photosphere. For a given stellar mass (M_*), the accretion rate was varied, and the values of parameter η were computed for which the PMS photosphere dominates over the viscous accretion disk and vice versa. Based on the values of parameter η, the CMD plane can be divided into regions of magnetospheric accretion regime and boundary layer accretion regime for a given M_*. For $\eta = 0$, the model, developed by Liu et al. (2022), degenerates into classical T Tauri star magnetospheric accretion regime. Comparing our absolute V versus $(V - I_C)$ CMD,[21] (Figure 4) with Figure 15 of Liu et al. (2022), we find after its first outburst V2493 Cyg has mostly resided over $\eta > 5$ region in the CMD plane. The $\eta > 5$ region signifies the region in the optical CMD plane where the circumstellar disk outshines the central PMS star, and all the observed spectral features originate from the disk itself. It is to be noted that, in $\eta > 5$ region, the magnetospheric accretion ceases, and the central PMS star accretes via the boundary layer accretion

Liu et al. (2022). Therefore, the reddening of the optical colors likely points toward the expansion of the emitting region around V2493 Cyg rather than the PMS star exiting the "FUor stage."

The color change observed in the present study can be further investigated using the reddening-invariant colors following the recipe of McGehee et al. (2004). The reddening-invariant colors take the generic form $Q_{xyz} = (x - y) - E(x - y)/E(y - z) \times (y - z)$, where x, y, and z are the observed magnitudes in respective filters. A color change "ΔQ_{xyz}" that is statistically distinct from 0 indicates changes in the SED that cannot be explained by changes in the extinction alone; rather, an intrinsic change (changes in temperature of the system) might have occurred in the SED. We have tabulated the values of reddening-invariant colors for $R_V = 3.1$ in Table 4. We see that there is a $>5\sigma$ change in the Q_{VRI} colors throughout the phase (6) period indicating an intrinsic change in the SED of V2493 Cyg.

The color change in the NIR wavelengths is less pronounced as compared to the optical bands. The left panel of Figure 5 shows the evolution of V2493 Cyg in the NIR CMD. The square box represents the pre-outburst quiescent phase locus of V2493 Cyg. The red dots represent the loci of V2493 Cyg during the 2010 outburst stage and its transition toward the intermediate quiescent phase as obtained from Leoni et al. (2010), Miller et al. (2011). The green dots represent the evolution of V2493 Cyg during our monitoring period. In the $J/J - K_S$ CMD, we see that there is a gradual slow transition toward redder color with very little change in J magnitude. The right panel of Figure 5 shows the evolution of V2493 Cyg in the NIR color–color (CC) plane of $J - H/H - K_S$. The position of V2493 Cyg in the NIR CC plane shows no significant extinction toward the source. We note that V2493 Cyg moved along the reddening vector in the phase (1) and (2) periods. During our monitoring period, which corresponds to phase (5) and phase (6), we note that the locus of V2493 Cyg is near to the Classical T Tauri (CTT) locus. From the NIR CC plane, we also note that there is no significant variation in the extinction of V2493 Cyg during phase (5) and phase (6). Thus, the NIR color evolution also reinforces our assumptions based on our reddening-invariant color analysis in the optical regime.

---

[21] We have obtained the values of isomass curves of Liu et al. (2022) using the online available plot digitizer tool at https://apps.automeris.io/wpd/. The obtained values are in the Gaia photometric system. The obtained photometric magnitudes and colors were then transformed to the Johnson–Cousins photometric system using the transformation equations between the Gaia photometric system and the Johnson–Cousins photometric system at https://gea.esac.esa.int/archive/documentation/GDR2/Data_processing/chap_cu5pho/sec_cu5pho_calib/ssec_cu5pho_PhotTransf.html.
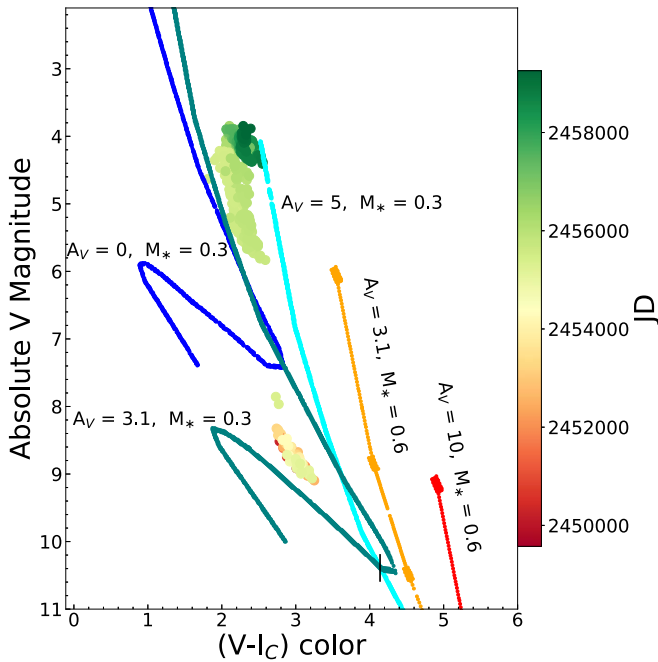
Figure 4. The plot shows the evolution of V2493 Cyg in the absolute magnitude V vs. $(V - I_C)$ color–magnitude diagram (CMD). The model isomass curves for mass 0.3 $M_\odot$, $A_V = 0$ mag, $A_V = 3.1$ mag, and $A_V = 5$ mag, and those for mass 0.6 $M_\odot$, $A_V = 3.1$ mag, and $A_V = 10$ mag are also plotted (Liu et al. 2022). The phase (6) locus of V2493 Cyg in the CMD plane shows that it currently lies above the $\eta > 5$ regime (marked by the vertical black red line), the regime where the circumstellar disk outshines the central PMS star so that all the spectral features that we observe are typical of the viscous accretion disk.

Table 4
Reddening-invariant Colors of V2493 Cyg during Our Monitoring Period

Days (JD)	Q_{VRI} (mag)	$N\sigma$	Days (JD)	Q_{VRI} (mag)	$N\sigma$
2457312	0.15	⋯	2458098	0.03	8.0
2457345	0.06	6.1	2458398	0.03	8.6
2457390	0.02	8.1	2458410	−0.01	10.1
2457660	0.07	5.9	2458449	0.05	7.3
2457670	0.09	4.1	2458456	0.04	8.2
2457708	0.04	8.1	2458792	0.01	10.3
2457976	0.11	1.7	2458794	0.01	10.4
2458448	0.07	5.8	2458813	0.05	7.2
2458473	0.11	1.6	2458817	0.05	6.9
2458624	0.11	2.8	2458826	0.01	10.1
2458040	0.01	9.7	2458834	0.01	8.7
2458069	0.02	8.6	2458848	0.04	8.1

Note. $N\sigma$ is the ratio of color change to the quadrature sum of measurement errors.

We have also investigated the color evolution in MIR W1 and W2 bands as obtained from the NEOWISE archive, and it is shown as a MIR CMD in the left panel of Figure 6. Interestingly, the MIR colors of V2493 Cyg have become bluer during our monitoring period. The blueing of the MIR colors can be possibly explained by the model developed by Liu et al. (2022). According to their model, at the outburst stage, the viscous disk temperatures are higher, therefore heating up the disk, which results in the blueing of the MIR colors. The gradual blueing might possibly hint at a gradual increase of the warm continuum emission (Liu et al. 2022).

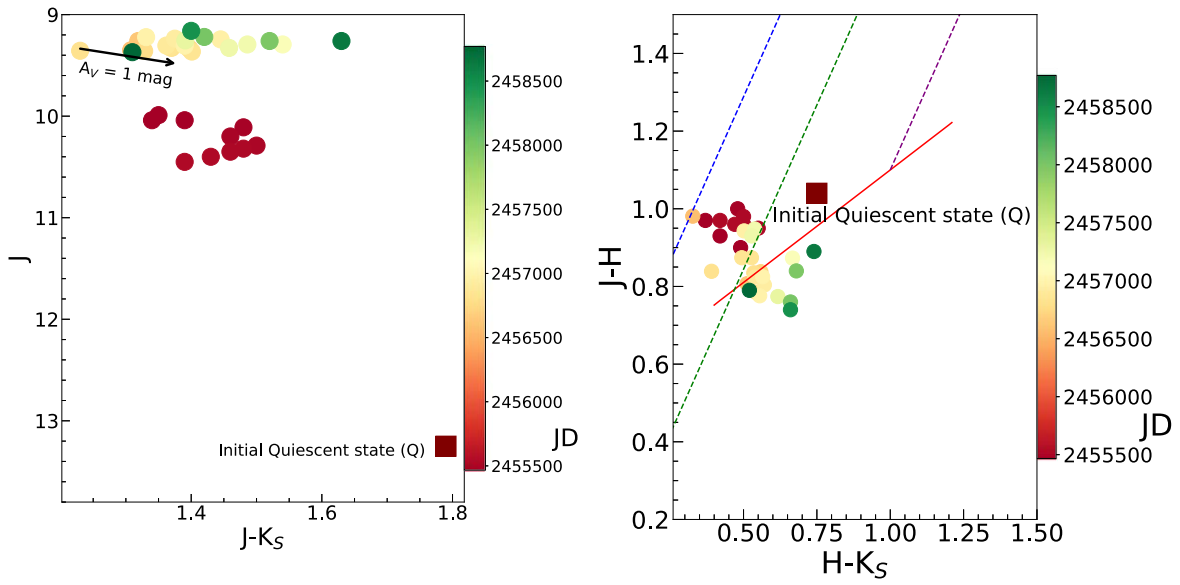### 3.3. The Evolution of Photometric Spectral Energy Distribution

The right panel of Figure 6 shows the multiepoch SEDs of V2493 Cyg during our monitoring period, i.e., phase (6). We have constructed the SEDs using the multiwavelength data (optical to MIR wavelengths, i.e., 0.44 μm (B), 0.48 μm (zg), 0.55 μm (V), 0.64 μm (zr), 0.65 μm (R), 0.80 μm (I), 3.4 μm (W1), and 4.6 μm (W2), taken from our observations and from the data archives of ZTF and NEOWISE). The details of the ZTF filter system are available in Bellm et al. (2018). Currently, we do not have any magnitude conversion system from the ZTF filter system to the Johnson–Cousins system. However, the ZTF system is calibrated using the Panoramic Survey Telescope and Rapid Response System (Pan-STARRS) data. We have therefore used the Tonry et al. (2012) relations to transform ZTF photometric data to the Johnson–Cousins photometric system. The magnitudes are then converted to the corresponding flux values using the online tool provided by the Gemini Observatory.[22] We hereby note that the data points used for the SED generation are not simultaneous but from nearby epochs.

During phase (6), the optical colors of the V2493 Cyg have become consistently redder (see Section 3.2). This implies a decrease in the strength of the physical process that triggered the second outburst. The multiepoch SEDs exhibit a change in the shape particularly in the MIR regime, which is in accordance with the blueing of the MIR colors due to the brightening of the disk by viscous heating.

3.4. Spectral Features

Figure 7 shows our continuum-normalized optical–NIR medium-resolution (0.4–2.4 μm) spectra of V2493 Cyg during our monitoring period. We can easily identify the absorption features, i.e., Hβ $\lambda4861$ Å, He I λ 5015 Å / Fe II $\lambda5018$ Å, Mg I at $\lambda5167$ Å / Fe II at $\lambda5169$ Å, Ba II $\lambda5853$ Å, Na I D resonance lines $\lambda5890/6$ Å, Fe II $\lambda6496$ Å, Hα λ 6563 Å, K I $\lambda7699$ Å, O I $\lambda7773$ Å, and Ca II infrared triplet (IRT) $\lambda8498$, $\lambda8542$, and $\lambda8662$ Å in the optical part of the spectrum. These absorption features are mostly blueshifted, which indicate that the powerful winds are coming out from V2493 Cyg (the wind velocities are discussed in detail in Section 3.7). One of the important spectral features that is not detected in our HFOSC spectrum is the Li I 6707 Å line. In FUors, this feature is observed in absorption. The presence of Li I confirms the PMS stage of FUors as lithium gets destroyed in the MS stage (Hartmann 1998). The absorption feature in Li I is also indicative of the shell-like features as observed in other bona fide FUors (Szabó & Kóspál 2021). The absence of Li I 6707 Å is likely because the spectral feature is too weak to be detected in our HFOSC spectrum. In the NIR wavelengths, we can identify several distinct absorption features, e.g., the CO (CO(2−0) and CO(3−1)) bandheads, Paschenβ (5−3) $\lambda1.28$ μm line, and He I 1.083 μm line. With the TANSPEC spectra, we can additionally identify a few more lines in absorption, like the Br (11−4) $\lambda1.68$ μm line, Paschenγ (6−3) $\lambda1.09$ μm, the Ca II IRT, O I $\lambda7773$ Å, and Hα. We have computed the equivalent widths "W_λ" of the important spectral lines and are listed in the Table 5. The evolutions of the profiles of the above lines during our spectroscopic monitoring period,

---

[22] https://www.gemini.edu/observing/resources/magnitudes-and-fluxes/conversions-between-magnitudes-and-flux

Figure 5. Left panel shows the $J − K_S$ color evolution of V2493 Cyg with J magnitude and time. The square represents the quiescent phase location of V2493 Cyg as obtained from the 2MASS survey on 2000 June 10. The dots represent the evolution of V2493 Cyg from phase (2) to phase (6) part of the LC. The red dots represent the evolution of V2493 Cyg during its transition to intermediate quiescent phase after the first outburst. Right panel shows the position of V2493 Cyg in the $J − H/$ $H − K_S$ CC diagram during our monitoring period corresponding to the post second outburst phase. The square represents the quiescent phase locus of V2493 Cyg in the CC plane. The solid red line represents the locus of the classical T Tauri (CTT) stars (Meyer et al. 1997). The blue, green, and maroon dashed lines represent the reddening vectors (Rieke & Lebofsky 1985).
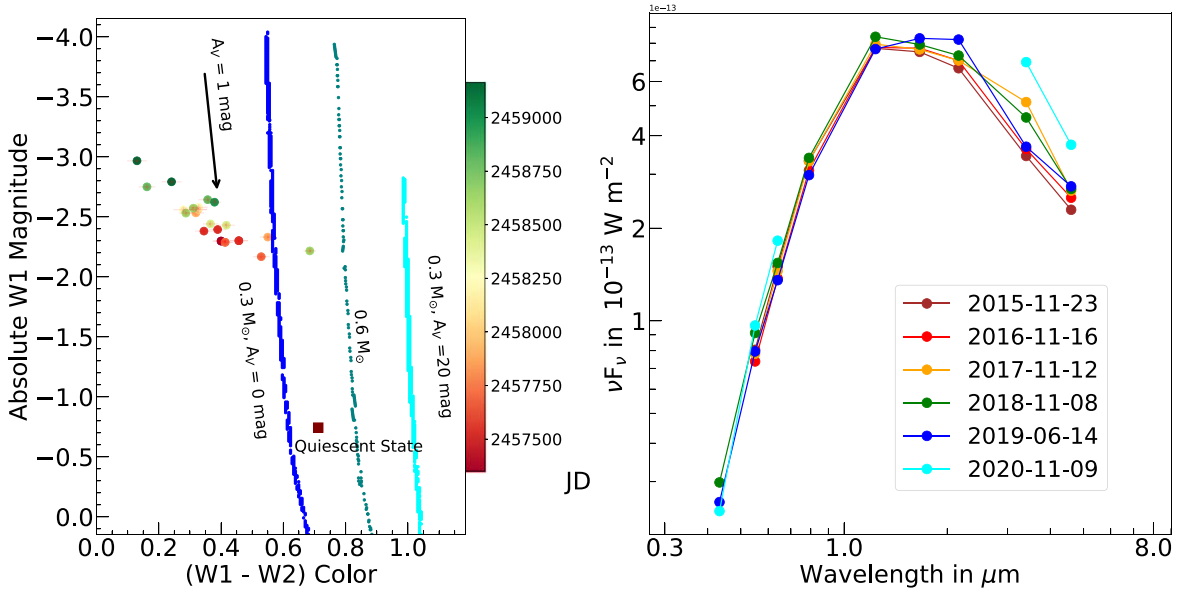
Figure 6. Left panel shows the W1 absolute magnitude vs. W1–W2 color evolution of V2493 Cyg with magnitude and time. The quiescent phase locus of V2493 Cyg is depicted by the brown square. The model isomass curves for mass 0.3 $M_\odot$, $A_V = 0$ mag, and $A_V = 20$ mag, and those for mass 0.6 $M_\odot$ are also plotted (Liu et al. 2022). The right panel shows the spectral energy distribution of V2493 Cyg during our monitoring period.

i.e., 2014 March 7 to 2021 June 14, are shown in Figure 8. Few of the optical lines, i.e., Hα, Ca II IRT, and O I lines, and NIR lines, i.e., CO bandheads, Paschen lines, He I 1.083 μm, which are important diagnostic tools for the accretion and outflow mechanisms, are discussed below.

3.4.1. Evolution of the Hα Line

The Hα line observed in YSOs originates from a variety of processes like accretion, outflowing winds, etc. Therefore, the time series analyses of the Hα line profile can help us to constrain the physical processes responsible for their origin

and variations (Hartmann et al. 1990). During our monitoring period, the line that showed the most riveting evolution is the Hα line. Previously, Miller et al. (2011) have found the Hα line to be in emission in their low resolution optical spectra taken on 2010 September 16 and 2010 November 2. However, during their monitoring period of 40 days, the Hα emission flux decreased by almost a factor of 0.5 from $\sim 2.8 \times 10^{30}$ to 1.5×10^{30} erg s^{-1}. The high resolution spectra of V2493 Cyg taken between 2010 to 2014 revealed the P Cygni profile of Hα line (Miller et al. 2011; Lee et al. 2015). The time evolution of Hα line from these spectra also showed a decrease in the emission peak of the P Cygni
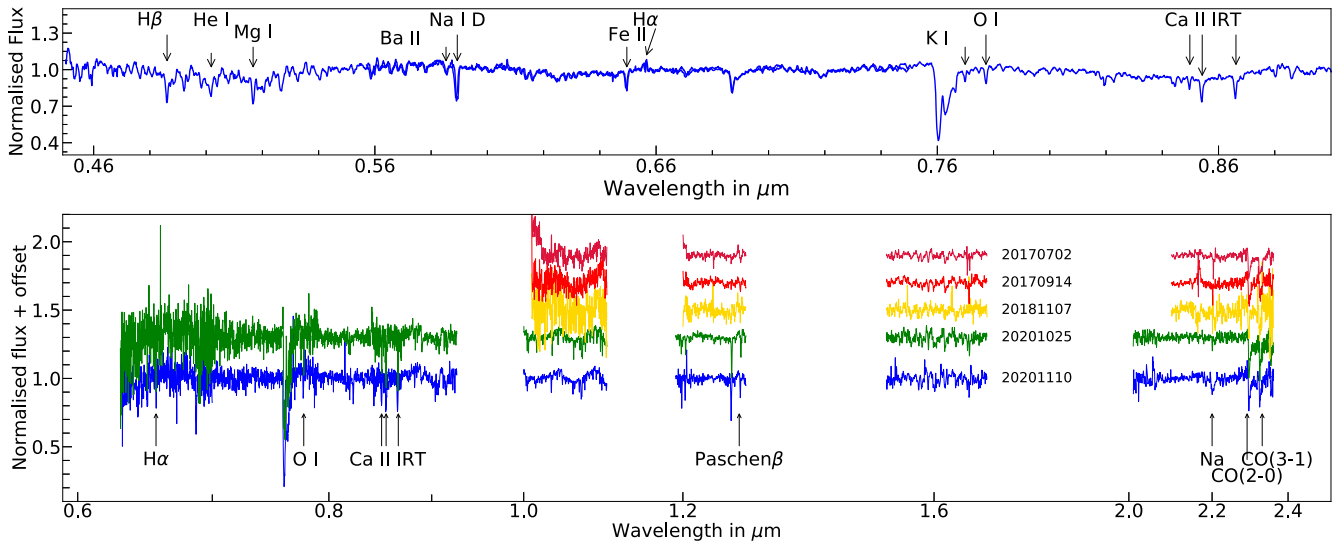
Figure 7. Sample of the normalized spectra of V2493 Cyg obtained during our monitoring period using HFOSC on 2 m HCT (∼0.4–0.9 μm; top panel), TIRSPEC (∼1.0–2.4 μm; bottom panel) on 2 m HCT, and TANSPEC (∼0.65–2.4 μm; bottom panel) on 3.6 m DOT. The lines that are used for the present study have been marked.

(The complete figure set of 48 images is available.)

Table 5
Variation of the Equivalent Widths of the Various Lines Identified in Our Study

Date	Julian Date	Hβ	Fe II 5018 Å	Mg I/Fe II 5167 Å /5169 Å	Ba II 5853 Å	Na I D	Fe II 6496 Å	K I 7699 Å	O I 7773 Å	Ca II IRT		
2015-05-17	2457160	⋯	⋯	⋯	0.8	3.7	1.4	0.6	1.3	0.9	2.2	1.5
2015-05-26	2457169	⋯	⋯	⋯	1.4	3.1	1.4	0.6	1.6	1.1	2.5	1.8
2015-06-10	2457184	3.3	2.7	2.5	1.3	3.2	1.6	0.6	1.7	0.9	2.2	1.8
2015-06-10	2457184	⋯	⋯	⋯	⋯	3.3	⋯	⋯	⋯	⋯	⋯	⋯
2015-08-18	2457253	2.9	2.5	2.6	1.0	3.5	1.5	0.6	1.6	1.4	3.4	1.9
2015-09-27	2457293	4.7	2.1	2.6	1.3	3.2	2.1	0.6	1.6	1.5	2.7	2.4
2015-10-12	2457308	3.1	2.3	2.2	1.2	3.1	1.4	0.6	1.3	0.9	2.0	1.9
2015-11-10	2457337	3.3	3.2	2.4	0.6	3.2	1.4	⋯	⋯	⋯	⋯	⋯
2016-01-20	2457408	2.3	3.0	2.5	1.4	3.5	1.7	0.5	1.3	1.0	1.9	1.7
2016-03-03	2457450	⋯	⋯	⋯	0.8	3.1	1.5	0.6	1.3	0.9	2.6	2.3
2016-03-15	2457463	3.4	2.8	2.4	0.9	3.2	1.4	0.5	1.3	1.0	2.0	2.2
2016-06-17	2457557	⋯	⋯	⋯	1.4	3.3	1.5	0.6	1.3	1.1	2.5	2.2
2016-07-24	2457594	3.2	2.6	3.2	1.7	3.7	1.4	0.6	1.4	0.6	1.6	1.3
2016-09-26	2457658	3.1	2.4	2.5	0.9	3.6	1.3	0.7	1.3	1.1	2.3	2.3
2016-10-05	2457667	⋯	⋯	⋯	0.8	3.3	1.4	0.6	1.6	1.1	2.5	2.1
2016-10-13	2457675	⋯	⋯	⋯	0.8	3.3	1.4	0.6	1.1	1.2	2.2	1.9
2016-11-17	2457710	4.2	2.5	2.6	0.9	3.3	1.3	0.5	1.4	1.2	2.5	2.1
2016-12-04	2457727	⋯	3.0	2.3	0.8	3.2	1.3	0.5	1.3	0.7	2.2	1.8
2016-12-08	2457731	3.6	2.8	2.3	0.7	3.0	1.6	0.7	1.4	0.9	2.4	2.0
2017-04-28	2457872	3.1	1.0	2.2	1.1	3.3	1.3	⋯	⋯	⋯	⋯	⋯
2017-07-03	2457938	1.9	1.6	2.1	1.1	3.4	1.2	0.7	1.0	0.5	1.8	1.7
2017-08-22	2457985	⋯	⋯	⋯	0.8	3.2	1.3	⋯	1.2	0.8	2.3	2.1
2018-08-13	2458344	3.4	⋯	2.2	0.9	3.2	1.3	0.4	1.4	0.9	2.3	1.7
2018-11-06	2458429	3.8	1.9	2.4	1.6	3.3	1.5	0.6	1.6	1.0	1.9	1.7
2018-11-21	2458444	⋯	⋯	⋯	⋯	⋯	⋯	⋯	⋯	⋯	⋯	⋯
2018-12-12	2458465	4.4	2.9	2.1	0.6	3.7	1.6	0.5	1.5	0.9	2.0	2.6
2018-12-25	2458478	3.9	3.3	2.3	0.7	3.2	1.5	0.6	1.7	0.9	2.3	1.8
2019-10-28	2458785	⋯	⋯	⋯	0.8	2.7	1.4	0.6	1.5	0.5	1.4	1.5
2021-06-14	2459380	4.9	2.1	2.1	0.7	3.3	1.5	⋯	1.1	0.5	1.6	1.6

Notes. The typical error in estimation of equivalent width is ∼0.2 Å by using the relation provided by Cayrel (1988). Equivalent widths are given in angstroms.

profile, particularly from 2013 onwards (see Figure 1 of Lee et al. 2015). This evolution of the Hα profile likely points toward the changing of the physical conditions responsible for the outflowing winds from regions close to the accretion (Hartmann et al. 1990; Kurosawa et al. 2006). We have started our spectroscopic monitoring of V2493 Cyg from
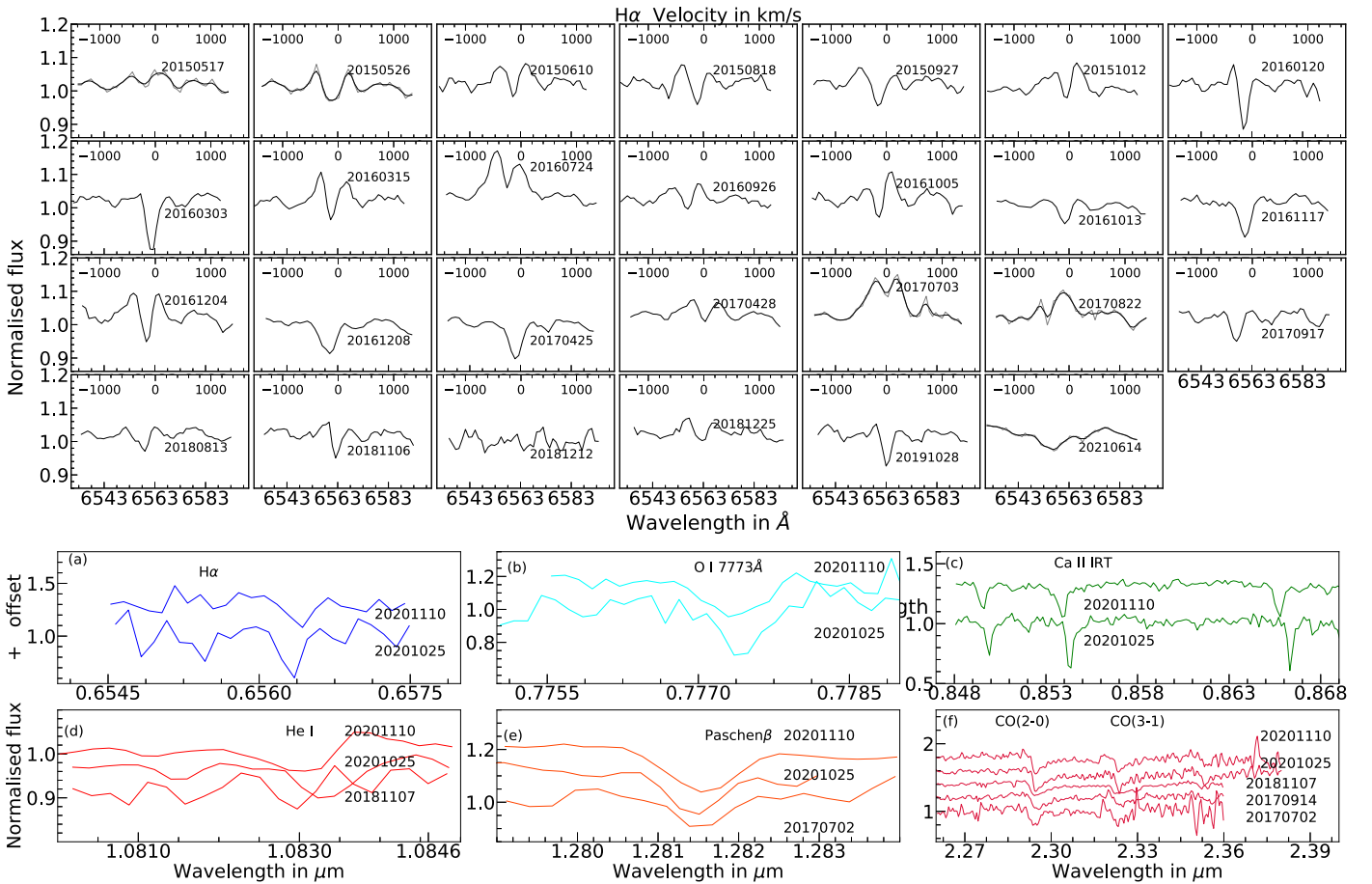
Figure 8. The time evolution of the different line profiles in the spectra of V2493 Cyg during our monitoring period.
(The complete figure set of 11 images is available.)

2015 May 17. The Hα line was present on 2015 May 17 with a primary peak at ∼6563 Å along with a secondary blue-shifted peak, which was about half of the primary peak's strength. This profile remained until 2015 June 10. The Hα line profile changed in the spectrum obtained on 2015 August 18 where the primary peak became half of the secondary blueshifted emission peak. The spectrum obtained on 2015 September 27 displayed a blueshifted absorption trough, which then changed to a self absorption profile as observed in the spectrum obtained on 2015 October 12. Spectra obtained on following epochs on 2016 January 20 and 2016 March 03 shows that the P Cygni profile changed to a absorption trough. Our spectra obtained on 2016 March 15 onwards until 2016 July 24 showed a Hα profile that is similar to the profile observed on 2015 August 18. The spectrum obtained on 2016 September 26 displayed a weak P Cygni profile, which became prominent in the spectrum taken on 2016 October 5. Subsequently, P Cygni profile disappeared, and an absorption trough appeared on 2016 October 13, and it remained until 2017 April 25. The absorption trough changed to a line profile displaying emission feature in the spectrum obtained on 2017 April 28. The observed emission profile is similar to the profiles previously observed on 2015 August 18 and 2016 March 15. The line profile of Hα as observed on the next two dates of observation, i.e., 2017 July 3 and 2017 August 22, is similar to the profile as observed on 2015 May 17. We then note the reappearance of the absorption feature starting from

2017 September 17 and remained in absorption until the end of our spectroscopic monitoring period, i.e., up to 2021 June 14 with one exception on 2018 December 12 where the Hα line was absent.

The variation in the line profile of Hα during our monitoring period indicates toward changes in the structure and/or speed of the outflowing winds originating from V2493 Cyg. Several of the Hα line profiles that we have observed during our monitoring period match with the atlas of Hα profiles as published by Reipurth et al. (1996). The variation of the Hα profile in T Tauri stars for a variety of scenarios has been previously studied in detail by Hartmann et al. (1990), Kurosawa et al. (2006). Emission profile in Hα as seen in the spectrum of Miller et al. (2011) corresponds to the Type I line profiles of the Reipurth et al. (1996) atlas. This type of line profile is reproduced in a accretion dominated regime with accretion rates in excess of $10^{-8}\ M_{\odot}\ \mathrm{yr}^{-1}$ with relatively weak disk winds, and the system is viewed in a high inclination (Kurosawa et al. 2006). It is worthwhile to mention here that Kóspál et al. (2011) calculated the inclination of the V2493 Cyg to be 73^{+6}_{-15} deg, which is regarded as a high inclination angle. The line profile observed on 2015 June 10 and similar profiles observed in other dates during our monitoring period are categorized as Type II-B in the Hα atlas. This type of profile is produced by the disk wind magnetosphere hybrid model of Kurosawa et al. (2006). The main feature of this line profile is high wind accelerations. The line profile observed on
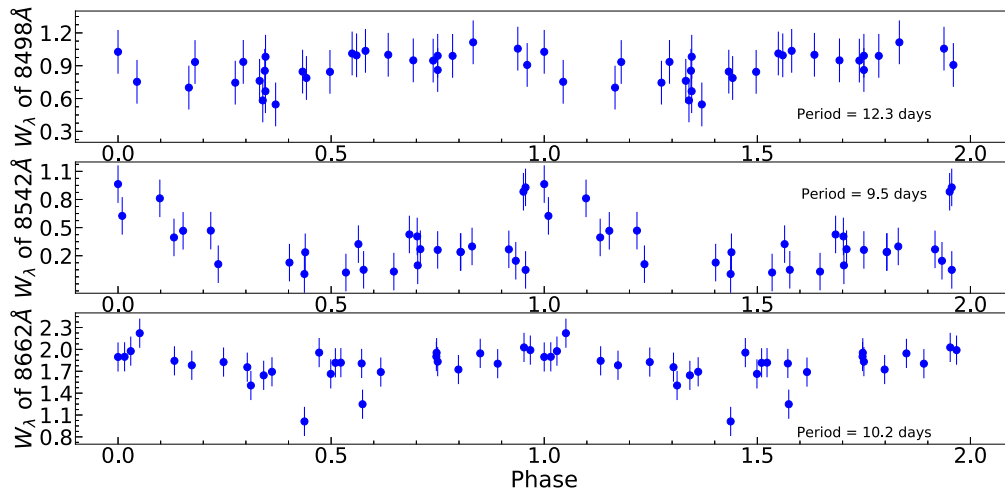
Figure 9. Folded phase plot of the W_λ of the Ca II IRT lines. The periods obtained are 12.3, 9.5, and 10.2 days, respectively, for $\lambda 8498$ Å, $\lambda 8542$ Å, and $\lambda 8662$ Å lines. The folding is done using the data obtained during our entire monitoring period. The obtained periodicities are calculated with a 2σ confidence label.

2016 March 15 and similar line profiles on the other dates of our monitoring period are classified as Type II-R (Type II-R line profile is defined as a line profile that consists of a secondary red peak whose strength is in excess of half the strength of the primary peak), according to the classification scheme of Reipurth et al. (1996). This type of line profile is also reproduced by the hybrid model of Kurosawa et al. (2006). According to this hybrid model, Type II-R is characterized by the decrease in wind acceleration. With the help of these hybrid models, we can also put a constrain on the temperature of the V2493 Cyg system to be 7500 K. We have also observed the P Cygni profile in Hα, which is attributed to outflowing winds from regions close to accretion. The evolution of Hα profile into a P Cygni feature from a self absorption feature can be possibly explained by the variations in the collimation of the outflowing winds as shown by the models of Kurosawa et al. (2006). We have also observed Hα to be in absorption on multiple dates during our monitoring period. The absorption features in Hα also help us to put a constrain on the temperature of the system. The temperature of the region producing absorption features in Hα is below 5000 K as evident from model (4) in Table 1 of Hartmann et al. (1990). The change in line profile from emission to absorption therefore indicates a change in temperature of the outflowing winds producing Hα (Hartmann et al. 1990; Kurosawa et al. 2006). This change in the outflowing wind structure can possibly be attributed to the small-scale photometric variations in the LC of V2493 Cyg, even though there is no significant change in the accretion rate as evident from the SEDs (see Section 3.3).
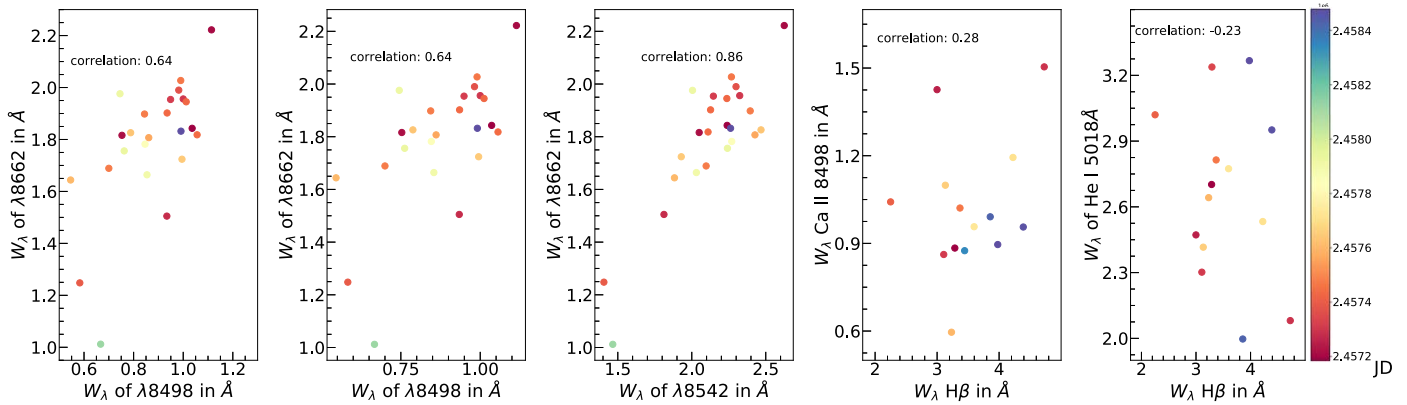
3.4.2. Ca II IR Triplet Lines

The Ca II IRT lines are found to be in absorption throughout our monitoring period. Previously, Ca II $\lambda 8498$ Å line displayed a P Cygni profile from 2010 to 2012 before transitioning to the absorption feature on 2013 April 21 (see bottom panel of Figure 1 of Lee et al. 2015). Combining our spectroscopic monitoring with that of Lee et al. (2015), we see that there is a gradual transition of Ca II $\lambda 8498$ Å line from the P Cygni profile to the absorption feature. This points toward the heavy outflow during our monitoring period. The profile of the Ca II IRT line $\lambda 8542$ Å is very similar to the isothermal wind models

(models (2)–(4)) developed by Hartmann et al. (1990). The models take into account a variety of system temperatures ranging from 20,000 to 5000 K. The Hα line profile variations as discussed in Section 3.4.1 are produced by systems having temperature in the range 5000–7500 K. Therefore, the models named as Model 3(I) and Model 4(I) are the likely models that can explain the observed profiles. This also helps us to constrain the density of the region to be around 10^{12} cm^{-3}.

The mean values of W_λ for the Ca II IRT lines are estimated as 0.8 ± 0.1, 2.2 ± 0.3, and 1.8 ± 0.2 Å. The low scatter values indicate that the density of the absorbing regions remained almost constant during our monitoring period. The ratio of the W_λ between 8542 Å and 8662 Å during our monitoring period is $2.2:1.8 = 1.2:1$. This value is lower than the intensity of the atomic transition strengths of these lines, which is 1.8:1, even after incorporating the error bars. Hence, the regions producing the absorption features of Ca II are not optically thin. This observed feature of Ca II spectral lines can be likely due to the high mass-loss winds from V2493 Cyg. The observed blueshifted absorption features in Na I D lines in the spectrum lend further credence to this scenario. This is because the Na I atom is easily ionized and is observed only in densest or high mass-loss rate wind models (Hartmann et al. 1990). We also searched for periodicities in the W_λ of the Ca II IRT lines. The periodicity search was done using the Period[23] software (Currie et al. 2014), which works upon the principle of Lomb−Scargle (LS) periodogram (Lomb 1976; Scargle 1982), to determine the period in the W_λ of the triplet. The advantage of the LS method is that it is effective even in case of the data set being nonuniformly sampled. We have also used the NASA Exoplanet Archive Periodogram[24] service for cross verification. The periods determined using both the softwares matched well. The periods obtained for the IRT lines are 12.3, 9.5, and 10.2 days, respectively. Figure 9 shows the phase folded data of the IRT lines covering our entire monitoring period. However, we note that the periodicities are calculated with a 2σ level of confidence; hence, we refrain from interpreting about its possible implications.

---

23 http://www.starlink.ac.uk/docs/sun167.htx/sun167.html
24 https://exoplanetarchive.ipac.caltech.edu/docs/tools.html

Figure 10. Figure showing the correlation between the W_λ of the different spectroscopic features of V2493 Cyg.

3.4.3. O I Line

The O I line at $\lambda7773$ Å is formed in the broad component regions (BCR), which corresponds to the warm gas in the envelope or the hot photospheres above the disk in the T Tauri stars. This is because the high energy state of O I $\lambda7773$ Å (~9 eV) prevents its formation in the photospheres of cool stars (Hamann & Persson 1992). Thus, O I $\lambda7773$ Å is an indicator of disk turbulence. In the previous studies on V1647 Ori and V899 Mon, Ninan et al. (2013, 2015) have shown that the W_λ of O I $\lambda7773$ Å varies significantly as the sources transitioned from the quiescent stages to the outburst stages. Therefore, continuous monitoring of O I line provides clues about the surrounding environment of the central source. The mean value of W_λ of O I at $\lambda7773$ Å during our monitoring period is estimated as 1.4 ± 0.2 Å. The scatter in the W_λ values is of the order of error in the estimation of W_λ, thereby, indicating that, after the second outburst, the inner glowing hot part of the disk has remained stable.

3.4.4. NIR Spectral Features

CO bandheads. The CO $(2-0)$ and $(3-1)$ bandhead spectral absorption features starting at $2.29\,\mu$m are one of the defining characteristics of FUors (Hartmann 1998). These overtone features are generally observed in many YSOs (either in emission or in absorption) and in giants. In the FUor and/or EXor family of sources, these bandhead CO features are believed to originate in the inner part of the heated disk where the temperature ranges between $2000\,\mathrm{K} < T < 5000\,\mathrm{K}$, and the density n_H is $> 10^{10}\,\mathrm{cm}^{-3}$ (Calvet et al. 1991; Kóspál et al. 2011b). As previously reported by Leoni et al. (2010) and Miller et al. (2011), the CO bandhead features in V2493 Cyg are in absorption. During our monitoring period also, we have found the CO bandhead features to be in absorption. The strength of the bandheads in absorption remained almost the same during our monitoring period. The absorption feature in CO bandheads therefore implies that the surface temperature of the inner part of the disk remained hotter than the middle layer of the disk (see Figure 7 of Calvet et al. 1991).

Metallic lines. The metallic line of Na $\lambda2.208\,\mu$m is not detected during our spectral monitoring. The Na $\lambda2.208\,\mu$m, if present, follows the profile of CO bandheads in K owing to their similar ionization potentials (Lorenzetti et al. 2009).

Paschen lines. We have also identified several Paschen lines in our NIR spectra. All the Paschen lines are found to be in absorption. The Paschenβ line is most prominent in the Paschen family and is observable in both the TIRSPEC and TANSPEC spectra. The absorption features present in Paschenβ are some of the defining characteristics of FUors (Connelley & Reipurth 2018). We could detect the Paschen $(6-3)$ spectral feature in our TANSPEC spectra. The Paschen lines are in absorption, therefore indicating their origin from the inner disk due to accretion and/or wind physics (Miller et al. 2011).

Brackett lines. The hydrogen Brackett $(11-4)$ line is detected in absorption. Previously, Leoni et al. (2010) have reported the observed absorption feature in the Brackett 11 line. During our monitoring period, we have observed a weak Brackett 11 absorption feature only once with TANSPEC in the spectrum obtained on 2020 October 25. This feature is also blueshifted, possibly indicative of similar origin like that of Paschen lines.

1.083 μm He I. During our monitoring period, we have also observed the absorption feature in He I 1.083 μm. This absorption feature is produced due to the resonant scattering of the 1.083 μm photons by the metastable triplet state of helium. This metastable state of helium is produced by the EUV to X-ray radiations due to accretion. The absorption feature of He I 1.083 μm is attributed to outflows generated due to accretion.

3.5. Correlation between Equivalent Width "W_λ" of Spectral Lines

The correlation between the W_λ of different spectral lines provides an important diagnostic tool to probe the physical association between different regions of a PMS star undergoing outburst (Hamann & Persson 1992; Ninan et al. 2013). This in turn help us in constraining and/or refining the various physical models that are used to describe these episodically accreting systems. Here, we have also tried to see the correlation (Pearson correlation coefficient) between the W_λ of various lines, and a few of them are shown in Figure 10.

The emission lines of the Ca II IRT originate from and/or near the accretion funnels in a magnetospheric accretion in low-mass YSOs (Muzerolle et al. 1998). Therefore, these emission lines are found to be tightly correlated as seen in the case of the V1647 Ori ($r = 0.88$; Ninan et al. 2013). In case of V2493 Cyg, the Ca II IRT lines are in absorption. The correlation between the absorption features of the Ca II IRT to our knowledge has not been studied before. We have calculated the correlation between the absorption features of the Ca II IRT (between W_λ of $\lambda8498$ Å with $\lambda8542$ Å or with $\lambda8662$ Å) and found that the coefficients are moderately
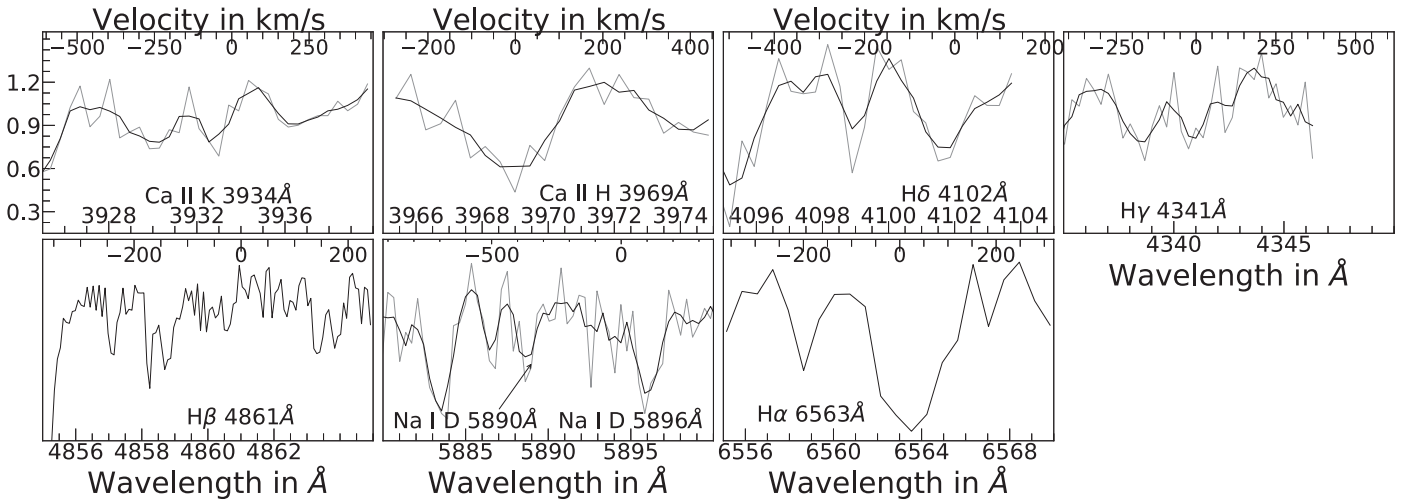
Figure 11. MRES spectra showing blueshifted absorption lines that are tracing the outflowing winds. The gray plot represents the original spectra, and the darker plot is the 3 pixel smoothed spectra of the original spectra.

correlated ($r \sim 0.6$). This moderate correlation is likely due to the additional physical process of the strong outflowing winds occurring with the magnetospheric accretion. The correlation coefficient between the W_λ of $\lambda 8542$ Å line and $\lambda 8662$ Å line is a bit tighter with $r = 0.86$.

We have found very weak correlations between the $\lambda 8498$ Å line of the Ca II IRT and Hβ line ($r \sim 0.2$) and Hβ and He I $\lambda 5015$ Å/Fe II $\lambda 5018$ Å lines ($r = -0.28$). This implies weak physical connection between these absorbing regions.

The Ca II IRT lines act as tracers of the accretion rate, while the O I $\lambda 7773$ Å is used as a proxy to monitor the disk turbulence. As both the lines originate in the BCR regions of the T Tauri stars (Hamann & Persson 1992), we investigated the correlation between these lines and did not find any. This could be due to no connection between the absorbing regions. We also did not find any correlation between the Na I D lines and the Fe II $\lambda 6496$ Å, which implies that the regions from which they originate are independent of each other.

3.6. Medium-resolution Echelle Spectra

The medium-resolution echelle spectra obtained from MRES displayed blueshifted absorption features that trace the outflowing disk winds. We can identify the Ca II H and K lines ($\lambda 3934$ Å and $\lambda 3969$ Å), Hδ $\lambda 4102$ Å, Hγ $\lambda 4341$ Å, Hβ, Na I D, and Hα lines, etc. The Ca II H and the Ca II K line is tracing a wind velocity of around -75 km s^{-1}. The outflowing wind velocities as traced by the hydrogen Balmer series lines, Hδ and Hγ, are -150 and -350 km s^{-1}, respectively. The wind velocity traced by Hβ is -250 km s^{-1}. Hα line is found to be in absorption. The absorption feature in Hα observed using MRES is consistent with the absorption feature that we observed in our HFOSC spectra from 2019 October 28 onwards. Both the Na I D lines at $\lambda 5890$ Å and $\lambda 5896$ Å are blueshifted and trace wind velocities of ~ -155 and -469 km s^{-1}, respectively. Figure 11 shows the plot of the outflowing wind features obtained from the MRES spectrum.

We also identify two neutral metallic lines Ca I $\lambda 6122$ Å and Fe I $\lambda 6142$ Å in our MRES spectrum (see top panel of Figure 12). Previously, Lee et al. (2015) had identified these two lines during their high resolution spectroscopic monitoring using Hobby–Eberly Telescope/High-Resolution
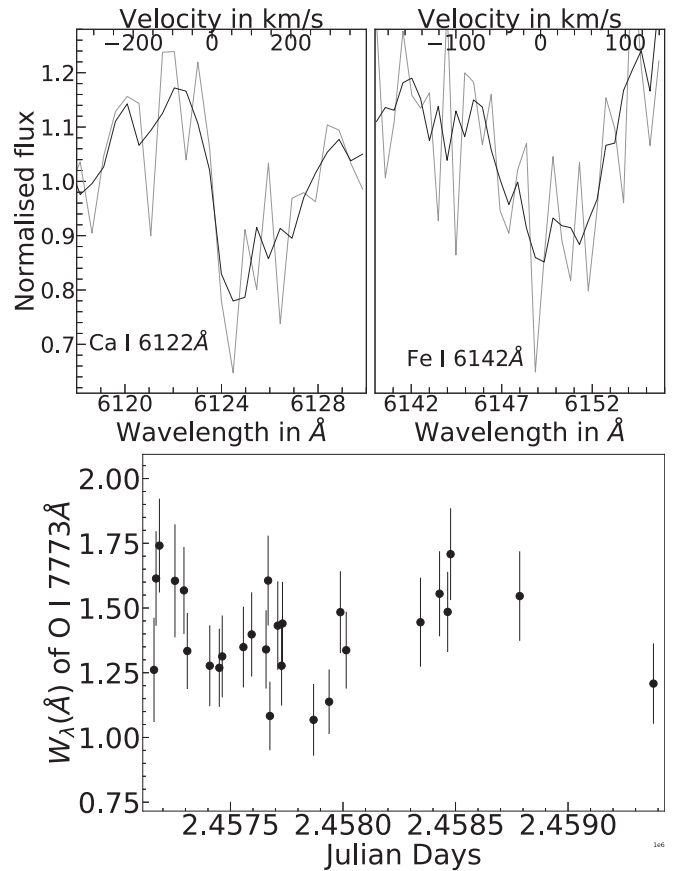
Figure 12. Top panel shows the MRES absorption lines of Ca I $\lambda 6122$ Å and Fe I $\lambda 6142$ Å, which show the evidence of disk rotation. The gray plot represents the original spectra, and the darker plot is the 3 pixel smoothed spectra of the original spectra. Bottom panel shows the evolution of the W_λ of O I $\lambda 7773$ Å line, which acts as a tracer for disk turbulence.

Spectrograph and attributed the presence of these lines as evidence for disk rotation. They further concluded from their spectroscopic monitoring about the steady rebuilding of the inner disk post outburst. Our detection of these two neutral metallic lines also points toward a similar conclusion. The bottom panel of Figure 12 shows the evolution of the O I

Table 6
The Variation of the Wind Velocity as Calculated from the Various Lines Identified in Our Study during Our Monitoring Period

Date	Julian Date	Hβ λ4861	He I/Fe II λ5015/λ5018	Mg I/Fe II λ5167/λ5169	Ba II λ5853	Na I D λ5890/6	Fe II λ6496	K I λ7699	Ca II IRT		
									λ8498	λ8542	λ8662
2015-05-17	2457160.267523	⋯	⋯	⋯	−20	−72	−68	−117	−82	−91	−89
2015-05-26	2457169.346111	⋯	⋯	⋯	−21	−66	−51	−46	−98	−111	−114
2015-06-10	2457184.332384	−66	−71	−29	⋯	−14	−70	−84	−94	−101	−112
2015-08-18	2457253.342766	−137	−110	−103	⋯	−54	−65	−94	−97	−129	−142
2015-09-27	2457293.279664	−84	−40	−14	−82	−78	−12	−86	−61	−65	−72
2015-10-12	2457308.150961	−53	−79	−40	⋯	−34	−20	−30	−50	−65	−77
2015-11-10	2457337.234954	−165	−193	−45	−70	−84	−12	⋯	−	⋯	⋯
2016-01-20	2457408.048056	−106	−154	−33	⋯	−75	−82	−99	−106	−107	−124
2016-03-03	2457450.448137	⋯	⋯	⋯	⋯	−13	⋯	−17	−47	−53	−72
2016-03-15	2457463.448137	−15	−75	−18	−13	−79	−51	−67	−88	−95	−94
2016-06-17	2457557.416366	⋯	⋯	⋯	−28	−78	−188	−199	−155	−169	−175
2016-07-24	2457594.171053	−106	−162	−16	−29	−86	−121	−91	−25	⋯	−10
2016-09-26	2457658.136389	−48	−37	−22	−18	−113	−40	−36	⋯	⋯	⋯
2016-10-05	2457667.278981	⋯	⋯	⋯	−46	−56	−93	−31	⋯	⋯	⋯
2016-10-13	2457675.187049	⋯	⋯	⋯	−103	−134	−169	−184	−105	−104	−100
2016-11-17	2457710.142685	−135	−231	−12	−158	−156	−50	−49	−25	−32	−30
2016-12-04	2457727.101065	⋯	−161	−83	−57	−56	−48	−115	−84	−73	−91
2016-12-08	2457731.166157	−71	−105	−64	−96	−52	−85	−53	−58	−51	−57
2018-08-13	2458344.283194	−85	−148	−59	−130	−22	−130	−124	−78	−72	−81
2018-11-06	2458429.140617	−101	−140	−15	−61	−56	−32	−51	−11	−36	−68
2018-12-12	2458465.125059	−24	−68	−67	⋯	−97	−56	−37	−19	−23	−17
2018-12-25	2458478.104021	−40	−73	−10	−114	−57	−16	−27	⋯	⋯	−56
2019-10-28	2458785.225682	⋯	⋯	⋯	−85	−31	−209	−172	−115	−111	−116
2017-04-25	2457869.32894	−68	−89	−62	−51	−67	−194	−160	−131	−134	−139
2017-04-28	2457872.27083	−90	−110	−44	−57	−27	−128	⋯	−	⋯	⋯
2017-07-03	2457938.32894	⋯	⋯	−29	−31	−17	−126	−36	⋯	⋯	⋯
2017-08-22	2457988.32894	⋯	⋯	⋯	−47	−174	−256	−175	−73	−81	−100
2017-09-17	2458014.32894	−198	⋯	−245	−95	−57	−221	−179	−78	−118	−99
2021-06-14	2459379.53727	−55	−142	−61	−28	−48	−118	−108	−102	−107	−87

Notes. Variation in wind velocity given in kilometers per second. The error in estimating the velocity is ∼25 km s^{-1}. The error is estimated by taking three independent measurements of the wavelength center and then calculating the standard deviation of the velocity, which is calculated from the wavelength shift..

λ7773 Å during our monitoring period. The variation of W_λ of the O I λ7773 Å is within the error bars, which therefore possibly implies toward the stabilization of the disk post the second outburst. The W_λ of O I 7773 Å is believed to be an indicator of disk turbulence (Hamann & Persson 1992).

3.7. Outflow Wind Velocities

Strongly blueshifted absorption lines are one of the defining characteristics of bona fide FUors. The wind features observed in V2493 Cyg varied with time during our monitoring period. We have calculated the outflow wind velocities of V2493 Cyg from several absorption lines, i.e., Hβ, He I λ5015 Å /Fe II λ5018 Å, Mg I λ5167 Å /Fe II 5169 Å, Ba II λ5853 Å, Na I D, Fe II λ6496 Å, K I λ7699 Å, and the Ca II IRT lines (Hartmann 1998), and these are listed in the Table 6. We have found variation in the shape of the Hβ line profile during our monitoring period. During our monitoring period, the Hβ line was not detected on 2016 June 17, but it reappeared on 2016 July 24. Hβ was undetected again on 2016 October 13 before reappearing again on 2016 November 17. The absorption profile of Hβ almost disappeared in 2016 December 4 while it reappeared prominently again on 2016 December 8. Similar behavior in the Hβ line evolution is again observed on 2018 December 12. The variation in the line profile of Hβ coincided with the line profile variations of Hα, therefore likely pointing toward a common origin. The shape of the line profile of He I λ5015 Å /Fe II λ5018 Å also varied during our monitoring

period. The He I λ5015 Å /Fe II λ5018 Å displayed an absorption profile until 2017 April 28. The absorption profile disappeared from our spectra on 2017 September 17 until the end of our monitoring period up to 2021 June 14. We interpret this disappearance with caution. The disappearance may be due to the spectral feature becoming too faint to be detectable in our spectrum.

During our monitoring period, the mean velocities of the Ca II IRT lines are -77 ± 35, -87 ± 35, and -88 ± 37 km s^{-1}, respectively. The mean velocities of Hβ, He I λ5015 Å /Fe II λ5018 Å, Mg I λ5167 Å /Fe II 5169 Å, Ba II λ5853 Å, Na I D, Fe II λ6496 Å, and K I λ7699 Å lines come out to be -86 ± 46, -115 ± 51, -50 ± 49, -62 ± 38, -67 ± 38, -103 ± 66, and -91 ± 55 km s^{-1}, respectively. The typical error in estimation of the velocities is ∼ 25 km s^{-1} (see Ghosh et al. 2022a); hence, the large scatters in the velocities imply intrinsic variations of the wind velocity as traced by the different lines. This observation is also supported by the Hα line profile variations as described in Section 3.4.1.

4. Discussion and Conclusion

V2493 Cyg is a bona fide FUor, which underwent its first outburst in the summer of 2010 and then transitioned to a short intermediate quiescent stage before rebrightening to maximum brightness in 2012 April. We have carried out our near simultaneous spectro-photometric monitoring from 2013 September 27 until 2021 June 14. During our monitoring period, in

particular, in the time period spanning between 2015 and 2019, V2493 Cyg dimmed by $\sim$0.6 mag in V band from its peak V-band magnitude on 2010 August at an average rate of $\sim$27.6 $\pm$ 5.6 mmag yr^{-1}. The average value of the decay rate for V2493 Cyg is of the same order as that of FU Ori and BBW 76 at 14 and 23 mmag yr^{-1}, respectively (Audard et al. 2014). The similar timescales of the decay rates therefore possibly point toward the occurrence of similar relaxing phenomenon in V2493 Cyg as that in FU Ori and BBW 76. This is typical behavior of FUor objects post outburst. The inner disk of FUor stars depletes, and it takes around $\sim$100 yr for the inner part of the disk to be completely depleted (Audard et al. 2014). Our simultaneous optical V-, R_C-, and I_C-band photometry revealed significant color changes in phase (6) compared to the previous phases with $V - R_C$ color and $V - I_C$ color becoming redder by 0.14 and 0.32 mag, respectively. This feature is also evident in the multiepoch SEDs where the slope at the optical regime has become steeper indicating reddening of the optical colors. The physical origins of the optical color evolution of V2493 Cyg were further studied using the recently developed theoretical models based on the optical CMD parameter space by Liu et al. (2022). The isomass curves divide the regions of the optical CMD plane into regions based on the nature of accretion. The evolution of optical colors during our monitoring reveals that V2493 is still accreting via the boundary layer accretion, the so-called *FUor regime*. Therefore, the reddening of the optical colors is likely due to the expansion of the emitting region around V2493 Cyg. A similar conclusion has been derived by Semkov et al. (2021) in their study. The NIR color evolution also follows the trend of the optical colors, which possibly hints toward a similar conclusion as that of the optical colors.

The most interesting photometric evolution of V2493 Cyg is its MIR color evolution. While the optical colors became redder in phase (6), we have found that the MIR colors W1–W2, obtained from the NEOWISE survey, became bluer. The blueing of the MIR colors as observed in the case of V2493 Cyg can be possibly attributed to the brightening of the disk due to the boundary layer accretion (Liu et al. 2022).

Combining our spectroscopic data with the previously published data by Lee et al. (2015), we see that there is a gradual transition from the P Cygni profile to absorption feature in the Ca II λ8498 Å line. The remaining two lines of the Ca II IRT are also found to be in absorption during our monitoring period. Such transition to the absorption features points toward the heavy outflow regime during our monitoring period. Combining the results of the evolution of Hα line during our monitoring period with that of Miller et al. (2011), we find that the emission feature evolved into Type II-B, Type II-R, P Cygni profile, and absorption features as categorized by the Hα atlas of Reipurth et al. (1996). Theoretical modeling of these variety of line profiles by Hartmann et al. (1990) and Kurosawa et al. (2006) reveals that the observed profiles are a result of the outflowing winds modulated by variable wind acceleration. The temperature of the systems also varies in between 5000 to 7500 K in the aforementioned different models. These variations can also be observed in the R-band LC of V2493 Cyg. We have also studied the evolution of the O I λ7773 Å line and found that the scatter in its W_λ is of the order of the error in estimation of W_λ. This implies possible stabilization of the disk after the second outburst. Previous studies on V1647 Ori and V899 Mon by Ninan et al. (2013, 2015) and Gaia 20eae by

Ghosh et al. (2022a) have revealed that this line acts as tracer of disk turbulence. Any sudden variations of the W_λ of O I λ7773 Å line point toward the possible transition between active and quiescent states. This view is also enhanced by the presence of the neutral metallic lines of calcium and iron at λ6122 and λ6142 Å, respectively, as observed in the MRES spectrum. These lines have attributed as signatures of disk rotation by Lee et al. (2015), which they stated as evidence for the steady rebuilding of the inner disk post the second outburst. The NIR spectra of V2493 Cyg consist of the blueshifted absorption features indicative of the outflowing winds from the source. The most notable of the spectral features that were not detected in the spectrum of V2493 Cyg is the Brγ 2.16 μm. Brγ is an important tracer of the accretion rate and is typically observed in highly accreting T Tauri stars; though, it is absent in many FUors (Ninan et al. 2015). In the NIR spectrum, we have detected the He I 1.083 μm feature. The He I 1.083 μm acts a proxy indicator for the outflowing winds generated due to the enhanced accretion rate (Ghosh et al. 2022a). Nondetection of the Brγ line in emission further reinforces the notion that V2493 Cyg is likely accreting via boundary layer accretion, which is in conformity with the evolution of V2493 Cyg in the optical CMD plane. The NIR spectroscopic features of CO bandheads display almost no variations during our monitoring. Therefore, it can be empirically stated that there has been no appreciable change in accretion rate post second outburst as the strength of the bandheads is directly related to the accretion rate (Calvet et al. 1991).

ORCID iDs

Arpan Ghosh ● https://orcid.org/0000-0001-7650-1870
Saurabh Sharma ● https://orcid.org/0000-0001-5731-3057
Joe P. Ninan ● https://orcid.org/0000-0001-8720-5612
Devendra K. Ojha ● https://orcid.org/0000-0001-9312-3816
D. K. Sahu ● https://orcid.org/0000-0002-6688-0800
Tapas Baug ● https://orcid.org/0000-0003-0295-6586
R. K. Yadav ● https://orcid.org/0000-0002-6740-7425
Puji Irawati ● https://orcid.org/0000-0002-3348-1491
Neelam Panwar ● https://orcid.org/0000-0002-0151-2361
Rakesh Pandey ● https://orcid.org/0000-0002-7485-8283
Tirthendu Sinha ● https://orcid.org/0000-0001-5508-6575
Aayushi Verma ● https://orcid.org/0000-0002-6586-936X

References

Astropy Collaboration, Robitaille, T. P., Tollerud, E. J., et al. 2013, A&A, 558, A33
Audard, M., Ábrahám, P., Dunham, M. M., et al. 2014, in Protostars and Planets VI, ed. H. Beuther et al. (Tucson, AZ: Univ. Arizona Press), 387
Baek, G., Pak, S., Green, J. D., et al. 2015, AJ, 149, 73
Bailer-Jones, C. A. L., Rybizki, J., Fouesneau, M., Demleitner, M., & Andrae, R. 2021, AJ, 161, 147
Bellm, E. C., Kulkarni, S. R., Graham, M. J., et al. 2018, PASP, 131, 018002
Calvet, N., Patino, A., Magris, G. C., & D'Alessio, P. 1991, ApJ, 380, 617
Cayrel, R. 1988, in IAU Symp. 132, The Impact of Very High S/N Spectroscopy on Stellar Physics, ed. G. Cayrel de Strobel & M. Spite (Dordrecht: Kluwer), 345
Cohen, M., & Kuhi, L. V. 1979, ApJS, 41, 743
Connelley, M. S., & Reipurth, B. 2018, ApJ, 861, 145
Currie, M. J., Berry, D. S., Jenness, T., et al. 2014, in ASP Conf. Ser. 485, Astronomical Data Analysis Software and Systems XXIII, ed. N. Manset & P. Forshay (San Francisco, CA: ASP), 391
Earl, N., Tollerud, E., Jones, C., et al. 2021, astropy/specutils: v1.2, v1.2, Zenodo, doi:10.5281/zenodo.4603801
Ghosh, A., Sharma, S., Ninan, J. P., et al. 2022a, ApJ, 926, 68
Ghosh, S., Ninan, J. P., Ojha, D. K., & Sharma, S. 2022b, pyTANSPEC: Python tool for extracting 1D TANSPEC spectra from 2D images, Astrophysics Source Code Library, ascl:2212.014
Kóspál, Á., Ábrahám, P., Acosta-Pulido, J. A., et al. 2011a, A&A, 527, A133
Kóspál, Á., Ábrahám, P., Acosta-Pulido, J. A., et al. 2016, A&A, 596, A52
Kóspál, Á., Ábrahám, P., Goto, M., et al. 2011b, ApJ, 736, 72
Green, J. D., Robertson, P., Baek, G., et al. 2013, ApJ, 764, 22
Hamann, F., & Persson, S. E. 1992, ApJS, 82, 247
Hartmann, L. 1998, Accretion Processes in Star Formation (Cambridge: Cambridge Univ. Press)
Hartmann, L., Calvet, N., Avrett, E. H., & Loeser, R. 1990, ApJ, 349, 168
Hartmann, L., Herczeg, G., & Calvet, N. 2016, ARA&A, 54, 135
Hartmann, L., & Kenyon, S. J. 1996, ARA&A, 34, 207
Herbig, G. H., & Bell, K. R. 1988, Third Catalog of Emission-Line Stars of the Orion Population (Santa Cruz, CA: Lick Observatory)
Kazarovets, E. V., Reipurth, B., & Samus, N. N. 2011, PZ, 31, 2
Kurosawa, R., Harries, T. J., & Symington, N. H. 2006, MNRAS, 370, 580
Landolt, A. U. 1992, AJ, 104, 340
Laugalys, V., Straižys, V., Vrba, F. J., et al. 2006, BaltA, 15, 483
Law, N. M., Kulkarni, S. R., Dekany, R. G., et al. 2009, PASP, 121, 1395
Lee, J.-E., Park, S., Green, J. D., et al. 2015, ApJ, 807, 84
Leoni, R., Larionov, V. M., Centrone, M., Giannini, T., & Lorenzetti, D. 2010, ATel, 2854, 1
Liu, H., Herczeg, G. J., Johnstone, D., et al. 2022, ApJ, 936, 152
Lomb, N. R. 1976, Ap&SS, 39, 447
Lorenzetti, D., Larionov, V. M., Giannini, T., et al. 2009, ApJ, 693, 1056
Mainzer, A., Bauer, J., Cutri, R. M., et al. 2014, ApJ, 792, 30
McGehee, P. M., Smith, J. A., Henden, A. A., et al. 2004, ApJ, 616, 1058
Meyer, M. R., Calvet, N., & Hillenbrand, L. A. 1997, AJ, 114, 288
Miller, A. A., Hillenbrand, L. A., Covey, K. R., et al. 2011, ApJ, 730, 80
Muzerolle, J., Hartmann, L., & Calvet, N. 1998, AJ, 116, 455
Ninan, J. P., Ojha, D. K., Baug, T., et al. 2015, ApJ, 815, 4
Ninan, J. P., Ojha, D. K., Bhatt, B. C., et al. 2013, ApJ, 778, 116
Ninan, J. P., Ojha, D. K., Ghosh, S. K., et al. 2014, JAI, 3, 1450006
Ojha, D., Ghosh, S. K., Sharma, S., et al. 2018, BSRSL, 87, 58
Reipurth, B., Pedrosa, A., & Lago, M. T. V. T. 1996, A&AS, 120, 229
Rieke, G. H., & Lebofsky, M. J. 1985, ApJ, 288, 618
Safron, E. J., Fischer, W. J., Megeath, S. T., et al. 2015, ApJL, 800, L5
Scargle, J. D. 1982, ApJ, 263, 835
Scholz, A., Froebrich, D., & Wood, K. 2013, MNRAS, 430, 2910
Semkov, E., Ibryamov, S., & Peneva, S. 2021, Symm, 13, 2433
Semkov, E. H., Peneva, S. P., Munari, U., et al. 2012, A&A, 542, A43
Semkov, E. H., Peneva, S. P., Munari, U., Milani, A., & Valisa, P. 2010, A&A, 523, L3
Sharma, S., Ghosh, A., Ojha, D. K., et al. 2020, MNRAS, 498, 2309
Sharma, S., Ojha, D. K., Ghosh, A., et al. 2022, PASP, 134, 085002
Stetson, P. B. 1987, PASP, 99, 191
Szabó, Z. M., Kóspál, Á., Ábrahám, P., et al. 2021, ApJ, 917, 80
Tody, D. 1986, Proc. SPIE, 627, 733
Tody, D. 1993, in ASP Conf. Ser. 52, Astronomical Data Analysis Software and Systems II, ed. R. J. Hanisch, R. J. V. Brissenden, & J. Barnes (San Francisco, CA: ASP), 173
Tonry, J. L., Stubbs, C. W., Lykke, K. R., et al. 2012, ApJ, 750, 99
Vorobyov, E. I., & Basu, S. 2006, ApJ, 650, 956
Yadav, R. K., Samal, M. R., Semenko, E., et al. 2022, ApJ, 926, 16